



HAL
open science

Wide band gap kesterite absorbers for thin film solar cells: potential and challenges for their deployment in tandem devices

Bart Vermang, Guy Brammertz, Marc Meuris, Thomas Schnabel, Erik Ahlswede, Leo Choubrac, Sylvie Harel, Christophe Cardinaud, Ludovic Arzel, Nicolas Barreau, et al.

► To cite this version:

Bart Vermang, Guy Brammertz, Marc Meuris, Thomas Schnabel, Erik Ahlswede, et al.. Wide band gap kesterite absorbers for thin film solar cells: potential and challenges for their deployment in tandem devices. *Sustainable Energy & Fuels*, 2019, 3 (9), pp.2246-2259. 10.1039/c9se00266a . hal-02291073

HAL Id: hal-02291073

<https://hal.science/hal-02291073>

Submitted on 5 Apr 2024

HAL is a multi-disciplinary open access archive for the deposit and dissemination of scientific research documents, whether they are published or not. The documents may come from teaching and research institutions in France or abroad, or from public or private research centers.

L'archive ouverte pluridisciplinaire **HAL**, est destinée au dépôt et à la diffusion de documents scientifiques de niveau recherche, publiés ou non, émanant des établissements d'enseignement et de recherche français ou étrangers, des laboratoires publics ou privés.

1 WIDE BAND GAP KESTERITE ABSORBERS FOR THIN FILM SOLAR CELLS:
2 POTENTIAL AND CHALLENGES FOR THEIR DEPLOYMENT IN TANDEM DEVICES

3
4 Bart Vermang^{1,2,3}, Guy Brammertz^{1,2,3}, Marc Meuris^{1,2,3}, Thomas Schnabel⁴, Erik Ahlswede⁴,
5 Leo Choubrac⁵, Sylvie Harel⁵, Christophe Cardinaud⁵, Ludovic Arzel⁵, Nicolas Barreau⁵,
6 Joop van Deelen⁶, Pieter-Jan Bolt⁶, Patrice Bras⁷, Yi Ren⁷, Eric Jaremalm⁷, Samira Khelifi^{8,9},
7 Sheng Yang⁸, Johan Lauwaert⁸, Maria Batuk¹⁰, Joke Hadermann¹⁰, Xeniya Kozina¹¹,
8 Evelyn Handick¹¹, Claudia Hartmann¹¹, Dominic Gerlach¹², Asahiko Matsuda¹³,
9 Shigenori Ueda^{14,15}, Toyohiro Chikyow^{12,13}, Roberto Félix¹¹, Yufeng Zhang^{11,16},
10 Regan G. Wilks^{11,17}, and Marcus Bär^{11,17,18,19}

11
12 ¹imec division IMOMEc – partner in Solliance, Wetenschapspark I, 3590 Diepenbeek,
13 Belgium

14 ²Hasselt University – partner in Solliance, Martelarenlaan 42, 3500 Hasselt, Belgium

15 ³EnergyVille, Thorpark 8320, 3600 Genk, Belgium

16 ⁴ZSW, Meitnerstrasse 1, 70563 Stuttgart, Germany

17 ⁵Institut des Matériaux Jean Rouxel (IMN), Université de Nantes, CNRS, 2 rue de la
18 Houssinière, 44322 Nantes, France

19 ⁶TNO – partner in Solliance, High Tech Campus 21, 5656 AE Eindhoven, The Netherlands

20 ⁷Midsummer AB, Elektronikhöjden 6, 175 43 Järfälla, Sweden

21 ⁸Department of Electronics and Information Systems (ELIS), Ghent University,
22 Technologiepark Zwijnaarde 15, 9052 Gent, Belgium

23 ⁹Department of Solid State Sciences, Ghent University, Krijgslaan 281-SI, 9000 Gent,
24 Belgium

25 ¹⁰Electron Microscopy for Materials Science (EMAT), University of Antwerp,
26 Groenenborgerlaan 171, 2020 Antwerp, Belgium

27 ¹¹Department Interface Design, Helmholtz-Zentrum Berlin für Materialien und Energie
28 GmbH (HZB), Hahn-Meitner-Platz 1, 14109 Berlin, Germany

29 ¹²International Center for Materials Nanoarchitectonics (MANA), National Institute for
30 Materials Science (NIMS), 1-1 Namiki, Tsukuba, Ibaraki 305-0044, Japan

1 ¹³Research and Services Division of Materials Data and Integrated System (MaDIS), National
2 Institute for Materials Science (NIMS), 1-1 Namiki, Tsukuba, Ibaraki 305-0044, Japan

3 ¹⁴Synchrotron X-ray Station at SPring-8, National Institute for Materials Science (NIMS), 1-1-
4 I Kouto, Sayo-cho, Hyogo 679-5148, Japan

5 ¹⁵Research Center for Advanced Measurement and Characterization, National Institute for
6 Materials Science (NIMS), 1-2-1, Sengen, Tsukuba, Ibaraki 305-0047, Japan

7 ¹⁶College of Physical Science and Technology, Xiamen University (XMU), 361005, Xiamen,
8 China

9 ¹⁷Energy Materials In-Situ Laboratory Berlin (EMIL), Helmholtz-Zentrum Berlin für
10 Materialien und Energie GmbH (HZB), Albert-Einstein-Str. 15, 12489, Berlin, Germany

11 ¹⁸Department of Chemistry and Pharmacy, Friedrich-Alexander-Universität Erlangen-
12 Nürnberg, 91058 Erlangen, Germany

13 ¹⁹Helmholtz-Institute Erlangen-Nürnberg for Renewable Energy (HI ERN), 12489 Berlin,
14 Germany

15

16 CORRESPONDING AUTHOR – Bart Vermang, Martelarenlaan 42, 3500 Hasselt, Belgium

1 BROADER CONTEXT

2 The power conversion efficiency of the dominant single junction photovoltaic technology is
3 approaching its theoretical limit. Further progress, with higher efficiencies and lower cost,
4 requires improving current technologies in new ways, whilst using cheap, abundant materials.
5 An approach to increase the efficiency is the construction of double junction solar cells
6 combining a top and bottom cell in a tandem device. If an established technology – such as
7 crystalline silicon – is used for the bottom cell, a relatively wide band gap material is needed
8 for the top cell. An ideal top cell would be low-cost and be made of abundant, non-toxic
9 materials. Typical top cell candidates that have been presented have some significant
10 drawbacks: Perovskite top cells, for example, contain toxic elements and have well-known
11 stability issues. III-V top cells are well studied for concentrators, but are too costly for tandem
12 applications. In this contribution, we report on our detailed fundamental analysis of a new
13 candidate absorber material, namely high band gap kesterite films. The Sn in the standard
14 $\text{Cu}_2\text{ZnSn}(\text{S,Se})_4$ kesterite structure is replaced by Ge (or Si), increasing the band gap to a level
15 where it is of interest in tandem configurations. This study describes the potential and the
16 challenges that are involved with the use of wide band gap kesterite absorbers in future
17 tandem devices.

18

19 ABSTRACT

20 This work reports on developments in the field of wide band gap Cu_2ZnXY_4 (with X = Sn, Si
21 or Ge, and Y = S, Se) kesterite thin film solar cells. An overview on recent developments and
22 the current understanding of wide band gap kesterite absorber layers, alternative buffer layers,
23 and suitable transparent back contacts is presented. $\text{Cu}_2\text{ZnGe}(\text{S,Se})_4$ absorbers with absorber
24 band gaps up to 1.7 eV have been successfully developed and integrated into solar cells.
25 Combining a CdS buffer layer prepared by an optimized chemical bath deposition process
26 with a 1.36 eV band gap absorber resulted in a record $\text{Cu}_2\text{ZnGeSe}_4$ cell efficiency of 7.6 %,
27 while the highest open-circuit voltage of 730 mV could be obtained for a 1.54 eV band gap
28 absorber and a Zn(O,S) buffer layer. Employing InZnO_x or TiO_2 protective top layers on
29 $\text{SnO}_2:\text{In}$ transparent back contacts yields 85-90 % of the solar cell performance of reference
30 cells (with Mo back contact). These advances show the potential as well as the challenges of
31 wide band gap kesterites for future applications in high-efficiency and low-cost tandem
32 photovoltaic devices.

33

34 KEYWORDS

35 Thin-film solar cells, wide band gap, kesterite, germanium, semi-transparent

1
2
3
4
5
6
7
8
9
10
11
12
13
14
15
16
17
18
19
20
21
22
23
24
25
26
27
28
29
30
31
32
33
34
35
36

I. INTRODUCTION

World-record single-junction solar cell efficiencies of monocrystalline silicon-wafer (Si) and thin-film (TF) solar cells are 26.7 % and 22.9 % [1,2], respectively, thus approaching their theoretical (Shockley-Queisser) limit of 30 % under standard illumination conditions [3]. One approach to increase the efficiency of solar cells above this limit is the construction of tandem devices. A tandem device consists of two solar cells: a wide band gap (E_G) solar cell (in which the photovoltaically active absorber material has an optical band gap of 1.5-2.0 eV) harvests the high-energy photons and a small band gap solar cell (in which the absorber has a band gap of 1.0-1.5 eV) harvests the low-energy photons. This approach can lead to theoretical efficiencies of up to 44 % under 1-sun illumination [4].

With a band gap of 1.1 eV [4], Si-wafer-based devices are the ideal bottom cell candidate, but many prominent top cell candidates have issues related to abundance, toxicity, stability, or cost [5]. Therefore, we consider kesterite-based devices as potential top cells for tandem device applications, because $\text{Cu}_2\text{ZnSn}(\text{S,Se})_4$ -type kesterite solar cells are stable, made out of abundant and non-toxic components, and already achieve relatively high performance [1]. Depending on the $[\text{S}]/([\text{S}]+[\text{Se}])$ composition, the band gap of the kesterite absorber can be tuned between 1.0 and 1.5 eV [6]. Highest efficiencies for $\text{Cu}_2\text{ZnSn}(\text{S,Se})_4$ -based devices are achieved when absorbers with band gaps between 1.1 and 1.2 eV are employed [7], which is too low for efficient (top) tandem solar cell applications. However, (partially) replacing tin atoms with silicon or germanium atoms has the potential to result in kesterite absorbers with band gaps even above 1.5 eV [8,9]. This work aims to give an overview on the recent development and current understanding of (i) these wide band gap kesterite absorber layers, (ii) alternative (non-toxic) buffer layer candidate materials, and (iii) suitable transparent back contacts (TBCs) allowing tandem configuration. A summary of recently published results is complemented with new experimental findings and a theoretical study of the efficiency potential of devices based on wide band gap kesterite absorbers. Thus, the paper aims at covering all aspects of deploying kesterite wide-band gap absorbers as top cells in tandem solar cell applications in order to identify inherent bottlenecks that may limit device performance and present generally valid optimization approaches and first results to lay the foundation and pave the way for future more detailed studies that undeniably have to follow.

2. EXPERIMENTAL, RESULTS, AND DISCUSSION

2.1. ABSORBER LAYER

First, we give an overview of the absorber layer formation, in which two main approaches are applied, i.e. sequential evaporation (Section 2.1.1) and solution-based deposition (Section

1 2.1.2). The first approach (respective samples are henceforth called → *EVAP-sample*) is more
2 convenient to study different metal components and is, therefore, used to investigate the
3 replacement of Sn atoms with Si or Ge in $\text{EVAP-Cu}_2\text{ZnSn(S,Se)}_4$ absorber layers; while in the
4 second approach (→ *SOL-sample*), the focus is on the replacement of Sn with Ge and the
5 optimization of the involved wet chemistry. Note that there will inherently be variations in
6 properties of the kesterite absorbers deposited by the different methods (i.e., using sequential
7 evaporation or solution-based deposition), however the findings that are presented in the
8 manuscript – while not exactly transferrable – mainly relate to universally relevant conditions
9 that will arise in cell production regardless of the absorber deposition method.

10 2.1.1. EVAPORATION-BASED PROCESS

11 The polycrystalline absorber layers are fabricated using a two-step vacuum-based approach;
12 see Figure S1. Soda lime glass (SLG) substrates of 1.3 mm thickness are used, on which a 150-
13 nm-thick Si(O,N) diffusion barrier is first deposited, followed by a 400-nm-thick Mo layer.
14 The thin Si(O,N) diffusion barrier is deposited in order to avoid the diffusion of elements
15 from the glass substrate into the absorber. Early tests have shown that the evaporated
16 absorber quality is better if this diffusion barrier is added. On top of this substrate, a multilayer
17 of different metals is deposited using a Pfeiffer PLS 500 evaporation system. For accurate layer
18 thickness control, a quartz microcrystal balance is used. This metal multilayer is then annealed
19 in an Annealsys As-One 150 rapid thermal annealing system that is equipped with a 10 % H_2Se
20 (diluted in N_2) gas line and a 100 % H_2S gas line. This way, the layers are selenized or sulfurized
21 under a continuous flow of H_2Se or H_2S . During this selenization/sulfurization step, a
22 polycrystalline layer is formed with typical grain sizes in the order of 0.5 to 1 μm .

23 2.1.1.1. Si-BASED COMPOUNDS

24 We have used metal layer stacks, including Si, to explore the possibility of fabricating EVAP-
25 $\text{Cu}_2\text{ZnSiSe}_4$, $\text{-Cu}_2\text{Zn(Si,Sn)Se}_4$, $\text{-Cu}_2\text{SiSe}_3$, $\text{-Cu}_2\text{SiS}_3$, $\text{-Cu}_8\text{SiSe}_6$, and $\text{-Cu}_8\text{SiS}_6$ layers [10].
26 Unfortunately, the Si appears to be largely unreactive at processing temperatures below
27 600 °C, which is the maximum temperature allowed for SLG substrates. Only $\text{EVAP-Cu}_8\text{SiSe}_6$
28 and $\text{EVAP-Cu}_8\text{SiS}_6$ could be produced in a reliable way, without significant presence of
29 secondary phases, leading to polycrystalline absorber layers with high-intensity
30 photoluminescence (PL) peaks at energies of 1.35 (for $\text{EVAP-Cu}_8\text{SiSe}_6$) and 1.84 eV (EVAP-
31 Cu_8SiS_6) [11]. However, no functioning solar cells could be fabricated with these absorber
32 layers, as the doping seemed to be too high (in the order of 10^{18} cm^{-3} or higher), and the
33 minority carrier lifetime seemed to be lower than 0.2 ns, leading to functioning diodes but no
34 photocurrent. One observation that could also explain the absence of any photoactivity is the
35 formation of SiO_2 during absorber processing. Figure 1 shows hard x-ray photoelectron
36 spectroscopy (HAXPES) survey spectra of an $\text{EVAP-Cu}_8\text{SiS}_6$ sample before (black) and after
37 (red) sulfurization treatment. Upon sulfurization, the O and Na (most likely diffused from the

1 SLG substrate) contents increase. The inset shows the region of the Si 2s and S 2p core level
2 lines compared to reference positions of silicon compounds [12]. The Si 2s line of the
3 sulfurized layer stack shifts to higher binding energies compared to the Si 2s peak before
4 sulfurization. The comparison with the reference positions indicates the conversion of Si-Si
5 into Si-S₂ and/or Si-O₂ bonds. The fact that the S 2p line can only be clearly observed on a
6 magnified (x 25) scale together with the high O 1s intensity for the sample after sulfurization,
7 however, suggests that the surface region of the sulfurized sample has mainly a SiO₂ character,
8 which would prevent efficient charge carrier transport.

9 2.1.1.2. Ge-BASED COMPOUNDS

10 For the fabrication of polycrystalline EVAP-Cu₂ZnGeSe₄ layers, we have used 180 nm of Ge,
11 125 nm of Zn and 170 nm of Cu as starting layers [13]. These layer thicknesses were chosen
12 in order to end up with a Zn-rich and Cu-poor composition of the absorber layer, with
13 Cu/(Zn+Ge) = 0.9 and Zn/Ge = 1.05. This metal stack was then selenized for 15 minutes in a
14 continuous flow of H₂Se at a temperature of 460 °C. The resulting absorber layer is
15 polycrystalline with a typical grain size in the order of 500 nm. Figure S2 shows a cross-section
16 scanning electron microscopy (SEM) image of a finished solar cell stack, exemplifying the grain
17 morphology of the absorber as well as the other layers of the solar cell stack. A Bragg
18 Brentano X-ray diffraction (XRD) measurement of a finished absorber layer on a Mo back
19 contact clearly shows the Cu₂ZnGeSe₄ peaks with a small contribution of a ZnSe secondary
20 phase, as a small shoulder of the main Cu₂ZnGeSe₄ peaks at angles around 27.3 and 45.3
21 degrees, shown in Figure 2. Due to the Zn-rich nature of the absorber layer, the presence of
22 ZnSe secondary phase has to be expected. Cu_{2-x}Se and GeSe₂ secondary phases cannot be
23 identified within the accuracy of the XRD measurements. Also note that the peaks of the
24 ternary phase Cu₂GeSe₃ overlap with the main peaks of the Cu₂ZnGeSe₄ phase completely,
25 making it impossible to distinguish these phases by XRD. To visualize the secondary phases,
26 cross-section energy dispersive X-ray spectroscopy (EDX) elemental maps of the absorber
27 were acquired in scanning transmission electron microscopy (STEM) mode, shown in Figure
28 3. The observed regions of elemental inhomogeneities are attributed to ZnSe – which seems
29 to be present in large amounts at the top surface of the absorber – and Cu₂GeSe₃ / Cu_{2-x}Se
30 phases – which are present more at the grain boundaries and at the backside Mo interface.
31 Some of the absorbers were lift-off in order to record Raman spectra near the EVAP-
32 Cu₂ZnGeSe₄/Mo interface. Both sides (front absorber and at the back side, i.e. near the back
33 contact) were analyzed. At the front Cu₂ZnGeSe₄ side (as published in [29]), only Cu₂ZnGeSe₄
34 is clearly detected, but presence of Cu₂GeSe₃ and Cu_{2-x}Se cannot be excluded as their Raman
35 peaks overlap with Cu₂ZnGeSe₄. At the back side only 2H-MoSe₂ related peaks are observed.
36 Time and energy resolved photoluminescence measurements (not shown) reveal a PL peak
37 at an energy of about 1.36 eV, with a decay time in the order of 2 ns. The band gap of this

1 absorber is thus too small to be employed as a top cell of tandem devices. However, due to
2 the high throughput of the evaporation process route/equipment, a large number of respective
3 EVAP-Cu₂ZnGeSe₄ samples are available and were thus (for practical reasons and to allow for
4 good statistics) chosen for most of our optimization efforts with respect to the absorber
5 surface treatment (see Section 2.2.1), the buffer layer (see Section 2.2.2), and the TBC (see
6 Section 2.4).

7 2.1.2. Ge-BASED COMPOUNDS BY SOLUTION-BASED PROCESS

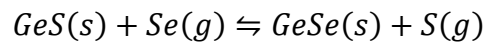
8 The SOL-Cu₂ZnGe(S,Se)₄ absorbers were deposited in a two-step process as schematically
9 drawn in Figure S3. A metal salt solution was deposited onto a Mo-coated SLG substrate by
10 doctor-blade coating with subsequent drying on a hot plate. Different solvents, metal salts
11 and chalcogen sources have been evaluated in a previous manuscript [14]. Here, the chemical
12 composition of the absorbers is Cu/(Zn+Ge)=0.7 and Zn/Ge=1.0 which is slightly more Cu-
13 poor than the EVAP-Cu₂ZnGeSe₄ layers. The chemical and electronic structure of respective
14 SOL-Cu₂ZnGe(S,Se)₄ absorbers and, in particular, the impact of the absorber formation by
15 annealing in Se-atmosphere has been monitored by lab-based soft x-ray photoelectron
16 spectroscopy (XPS) and synchrotron-based HAXPES. The XPS measurements were
17 performed in the off-synchrotron analysis chamber at EMIL in ultra-high vacuum (base
18 pressure < 5×10⁻¹⁰ mbar) employing a non-monochromatized Mg K_α (1253.56 eV) x-ray tube
19 (PREVAC RS40BI) as excitation source. The photoelectrons were detected by a Scienta
20 Omicron Argus CU electron analyzer. HAXPES was measured at beamline BL15XU at SPring-
21 8 using an excitation energy of 6 keV and a Scienta R4000 electron analyzer (see [15,16] for
22 more details on the experimental setup; same measurement conditions apply for the data
23 shown in Figure 1). Figure 4 shows the XPS S 2p/Se 3p (left panel) and HAXPES shallow core
24 level (right panel) spectra of a SOL-Cu₂ZnGe(S,Se)₄ sample prepared from a solution of Cu-,
25 Zn- and Ge-oxides in water and ammonium thioglycolate. Upon selenization, a clear Se 3d
26 signal in the shallow core level region and the Se 3p core level dominating the S 2p/Se 3p
27 energy region can be observed. The fit of the spectrum with S 2p and Se 3p doublets (see top
28 spectrum in Figure 4 – left panel) reveals the presence of at least two Se species, and two S
29 species – where the secondary (S) peak most likely indicates the presence of S-O_x and Se-O_x
30 (with x ≥ 3). The presence of Se-O_x is also indicated by the high-binding energy shoulder of
31 the Se 3d line in the shallow core level region (and depicted in the right panel of Figure 4).
32 Quantifying the fit results yields a (surface) [S]/([S]+[Se])-ratio of approximately 0.1,
33 significantly lower than the bulk composition of 0.3 [14]. The chemical environment of S in
34 the absorber precursor layer (i.e., before selenization) is also rather complex – as indicated
35 by the broad S 2p spectrum with a low binding energy shoulder (in the bottom spectrum in
36 Figure 4 – left panel), which significantly deviates from the expected spectral shape of a S 2p
37 doublet (see blue fit component on the top spectrum). The shallow core level photoemission

1 lines additionally reveal that the selenization process impacts the Zn/Cu ratio (the Cu 3p line
2 intensity is significantly increased) and the chemical bonding environment of Ge (see inset of
3 Figure 4 – right panel). Presumably, oxidized Ge is converted to form Ge-Se bonds upon
4 selenization. Finally, the location of the valence band maximum at 0.2 (± 0.1) eV (below the
5 Fermi level), indicated by the arrow in Figure 4 (right panel), is in agreement with a p-type
6 doped material, which can generally be observed for these kinds of absorbers.

7 To fabricate solar cells, CdS buffer layers are deposited by chemical-bath deposition (CBD)
8 followed by a sputtered ZnO and ZnO:Al layer. Although the band alignment of
9 $\text{Cu}_2\text{ZnGe}(\text{S,Se})_4$ with CdS is believed to be non-ideal, in a direct comparison with potential
10 alternative buffer layer candidate materials a CdS buffer was found to result in the highest
11 efficiencies [17]. The morphology of a SOL- $\text{Cu}_2\text{ZnGe}(\text{S,Se})_4$ absorber with CdS buffer can be
12 seen in the cross-section transmission electron microscopy (TEM) image displayed in Figure
13 S4(a). It shows two distinct layers within the SOL- $\text{Cu}_2\text{ZnGe}(\text{S,Se})_4$: larger grains on top and
14 smaller grains at the bottom. Note that the CdS layer on top of the absorber is only 50 nm
15 thick and therefore hard to identify in this image. All elements are for the most part
16 homogeneously distributed within the absorber layer; therefore, only the distribution of Zn
17 signal is shown in Figure S4(b), where some brighter spots in the large-grain layer can be seen,
18 which we interpret as indication for the presence of a $\text{Zn}(\text{S,Se})_2$ secondary phase. Additionally,
19 the signal of carbon residues that arise from thiourea is displayed in Figure S4(c). Here carbon
20 is only present in the small-grain layer, whereas the large-grain layer is mostly carbon-free.
21 With a higher magnification (not shown), an amorphous layer covering the $\text{Cu}_2\text{ZnGe}(\text{S,Se})_4$
22 particles can be seen. The distribution of Cd [Figure S4(d)] shows that, in contrast to other
23 investigations of kesterite absorbers with a CBD-processed CdS buffer [18], no major
24 diffusion of Cd into the absorber layer can be detected.

25 Our standard solution-based deposition approach results in SOL- $\text{Cu}_2\text{ZnGe}(\text{S,Se})_4$ absorber
26 material with a band gap of around 1.5 eV [14]. For application in tandem solar cells, a slightly
27 higher absorber band gap would be advantageous. One possible means to increase the band
28 gap would be a partial or complete cation substitution, e.g., Si for Ge [9], Ag for Cu [19], or
29 Ba for Zn [20]. However, a more complicated phase diagram is expected when using
30 additional elements, and so we focus on increasing the band gap by tuning the anion
31 composition (i.e., the $[\text{S}]/([\text{S}]+[\text{Se}])$ -ratio), a well-established method for $\text{Cu}_2\text{ZnSn}(\text{S,Se})_4$
32 absorbers. In general, the anion composition can be controlled (i) in the metal salt solution
33 and/or (ii) during the annealing process. It is used in slight excess to ensure that enough S is
34 present to form the kesterite phase during the drying step on a hot plate. If one would like
35 to lower the band gap of the SOL- $\text{Cu}_2\text{ZnGe}(\text{S,Se})_4$ absorber, thiourea could partly or
36 completely be replaced by selenourea to decrease the $[\text{S}]/([\text{S}]+[\text{Se}])$ -ratio or fabricate S-free
37 SOL- $\text{Cu}_2\text{ZnGeSe}_4$ absorbers. However, further increasing the amount of thiourea would only

1 lead to excess chalcogen that cannot be incorporated into the kesterite lattice (and also more
2 residual carbon and nitrogen) and does, therefore, not lead to an increase of the
3 $[S]/([S]+[Se])$ -ratio and thus absorber band gap. Therefore, we focus on increasing the
4 $[S]/([S]+[Se])$ -ratio during the annealing step, following approach (ii). The most obvious
5 procedure would be to anneal the sample in the simultaneous presence of Se and S. However,
6 the boiling point of S is 445°C [21], considerably lower than the annealing temperature of
7 550°C, and thereby does not allow a constant S supply during the annealing. Therefore, GeS
8 is used as an additional sulfur source [22], which is expected to release S into the gas phase
9 via the following reaction:



11 To allow for fine-tuning of the absorber band gap, the amount of GeS was varied between 0
12 and 100 mg. As a result, S is incorporated into the kesterite lattice, as can be seen from the
13 shift of the 112-reflection in the XRD patterns displayed in Figure 5. Using Vegard's law the
14 $[S]/([S]+[Se])$ -ratio can be estimated based on this data, revealing that it varies in a range
15 between 0.27 and 0.50 [22]. However, the peak shape of the 112-reflections slightly changes
16 with the amount of GeS. Starting from 40 mg (resulting in an absorber with a band gap of 1.67
17 eV [22]), a shoulder at higher diffraction angles is visible, indicating the coexistence of an
18 orthorhombic phase that is known to occur for high $[S]/([S]+[Se])$ -ratios in $Cu_2ZnGe(S,Se)_4$
19 absorbers [23].

20 To evaluate the influence on the solar cell performance, the current density-voltage [i.e., $J(V)$]
21 characteristics of the best solar cells from SOL- $Cu_2ZnGe(S,Se)_4$ absorbers with external
22 quantum efficiency (EQE)-derived band gaps of 1.5, 1.6 and 1.7 eV (corresponding to
23 $[S]/([S]+[Se])$ -ratios of 0.27, 0.39, and 0.50, respectively) are compared in Figure 6; the
24 corresponding cell parameters are listed in Table 1. As expected, the short-circuit current
25 density (J_{sc}) decreases with increasing absorber band gap. The open circuit voltage (V_{oc})
26 increases considerably from 617 to 683 mV when the absorber band gap is increased from
27 1.5 to 1.6 eV, but decreases for the 1.7 eV absorber. The fill factor (FF) shows a slight decrease
28 with absorber band gap, and efficiency reducing from 6.0 to 2.7 %. The loss in V_{oc} for devices
29 based on absorbers with a band gap larger than 1.6 eV represents the most crucial loss in this
30 sample series, which might be linked to the above-mentioned coexistence of a kesterite and
31 an orthorhombic phase. However, the band alignment between absorber and buffer layer
32 might also become severely performance limiting, especially for solar cells based on 1.7 eV
33 band gap $Cu_2ZnGe(S,Se)_4$ absorbers. To make these absorbers viable for application as top
34 cells for tandem configurations, significant efficiency enhancements are required (see
35 discussion below). In order to achieve this improvement of wide band gap kesterite solar cell
36 efficiencies, an optimization of all layers in the TF layer stack, especially the buffer/absorber
37 interface, has to be performed (see Section 2.2).

2.2. SURFACE TREATMENT AND BUFFER LAYER OPTIMIZATION

For the absorber layers discussed in Section 2.1, two paths toward optimization of performance were pursued: (i) selective etching of the ZnSe secondary phases (mentioned in Section 2.1.1.2) was successfully carried out and the impact on the final solar cell properties was determined (as discussed in Section 2.2.1). (ii) The CdS buffer layer deposition was optimized, and the employment of alternative buffer layers evaluated (as discussed in Section 2.2.2). Due to its better availability this work – unless stated otherwise – was done on evaporated EVAP-Cu₂ZnGeSe₄ absorbers.

2.2.1. ABSORBER SURFACE TREATMENT

Various absorber characterizations techniques reveal the presence of ZnSe at the surface of EVAP-Cu₂ZnGeSe₄ kesterites prepared by the two-step process of evaporating metal layers in vacuum with subsequent selenization of the layer stack (detailed in Section 2.1.1.2). The presence of secondary phases at the absorber/buffer interface is usually reported to have a deleterious effect on the efficiency of the resulting solar cells [24]. To prevent this, a (selective) chemical etching process for ZnSe is included as part of the standard procedure to prepare efficient solar cells. To find the proper etching procedure, we identified two previously reported etching strategies: (i) acidic etching with hot HCl, and (ii) an oxidation route at room temperature with KMnO₄ in a sulfuric acid medium [25]. Raman spectroscopy with an excitation wavelength of 458 nm allows detection of even small traces of ZnSe due to the resonant measurement conditions (i.e., excitation energy is close to the band gap of ZnSe, ≈ 2.7 eV) [26], hence, (resonant) Raman spectroscopy was used as the main characterization tool to aid in determining the optimal experimental etching conditions (temperature, concentration, duration) that result in a ZnSe-free EVAP-Cu₂ZnGeSe₄ surface. For approach (i), this means etching with a 12 wt% HCl solution, see Figure 7. For approach (ii), a 2-minute etch at room temperature in an aqueous solution of 1 mol/L KMnO₄ in 1 mol/L H₂SO₄ is sufficient to effectively remove ZnSe. Ultimately, the HCl etching was chosen as the standard etching procedure based on practical arguments (parameter control, processing, and solution stability). The optimized HCl etching conditions used in standard solar cell manufacturing have been determined to be: 15 min etching in a 12 wt% HCl solution at a temperature of 80 °C.

Solar cells were prepared based on EVAP-Cu₂ZnGeSe₄ absorbers (from the same batch) grown on Mo coated Si(O,N)/SLG, followed by CBD of CdS buffer layer, sputtering of an i-ZnO/ZnO:Al window bi-layer and finalized by e-beam deposition of Ni/Al/Ni grids for the front contact. Two absorbers served as references (i.e., not etched) and three were HCl treated at 60, 70, and 80 °C. Resonant Raman spectra confirm that only the untreated

1 references contain ZnSe at the surface. The effect of this etching procedure on V_{OC} , FF, and
2 EQE are presented in Figures 8 and 9. The V_{OC} of the cells prepared with untreated references
3 are in the range of 500-550 mV, which corresponds to 45-50 % of the maximum achievable
4 V_{OC} ($V_{OC,max}$) for such an absorber band gap (i.e., PL peak at 1.36 eV). In comparison, high-
5 efficiency $Cu_2ZnSn(S,Se)_4$ solar cells typically achieve 55-60% of $V_{OC,max}$ [27]. The lower V_{OC}
6 observed here with Ge-kesterite solar cells is suspected to partially originate from a non-ideal
7 buffer/absorber interface (allowing for charge carrier recombination). The presence of ZnSe
8 on the surface of the absorber (or at the buffer/absorber interface) may explain the losses.
9 This explanation is supported by the fact that V_{OC} is significantly improved for solar cells for
10 which the EVAP- $Cu_2ZnGeSe_4$ absorber underwent prior HCl etching (resulting in a ZnSe free
11 absorber surface), reaching around 55 % of $V_{OC,max}$. Despite this significant V_{OC} improvement,
12 solar cells prepared with HCl-treated absorbers result in lower efficiencies due to a dramatic
13 FF loss and an EQE drop at longer wavelength (usually ascribed to a reduced collection length).

14 To determine the origin of the FF and collection length losses after HCl etching, surface
15 characterization by HAXPES has been performed at the HiKE endstation [15] equipped with
16 a Scienta R4000 electron analyzer and located at the BESSY II KMC-I beamline [16] at HZB,
17 using an excitation energy of 2.1 keV. The HAXPES survey spectra of an as-deposited (i.e.,
18 not etched; black spectrum) and a HCl etched EVAP- $Cu_2ZnGeSe_4$ sample (red spectrum) are
19 shown in Figure 10. All $Cu_2ZnGeSe_4$ -related photoemission and Auger lines can be observed,
20 as expected. In addition, signals related to oxygen (O 1s), carbon (C 1s), and for the as-
21 deposited EVAP- $Cu_2ZnGeSe_4$ also cadmium (Cd 3d) can be observed. The presence of oxygen
22 and carbon can be attributed to a surface contamination layer formed due to the (short) air
23 exposure of the samples. The significant increase of the C 1s line upon HCl etching is most
24 likely related to additional contamination during the etching procedure. The presence of
25 cadmium on the as-deposited sample is ascribed to cross contamination from CdS/EVAP-
26 $Cu_2ZnGeSe_4$ samples that have been transported in the same sample box. Due to these varied
27 and significant states of surface contamination, we deliberately refrain from attempting to
28 quantify the HAXPES data but rather discuss them qualitatively. The HAXPES survey spectrum
29 of the as-deposited EVAP- $Cu_2ZnGeSe_4$ sample is dominated by Zn and Se signals. Upon HCl
30 etching, the Zn- and Se-related signals are significantly reduced, and the Cu/Zn ratio is
31 enhanced, in good agreement with the Raman results discussed above, i.e. the presence of a
32 ZnSe (surface) phase before etching and its removal upon HCl-treatment. The inset of Figure
33 10 shows the related detail spectra of the Se $3d_{3/2}$ and $3d_{5/2}$ spin-orbit split doublet, having a
34 separation between 0.8 and 0.9 eV. The spectral shape of the Se 3d line significantly changes
35 upon HCl etching. For the HCl-etched EVAP- $Cu_2ZnGeSe_4$ sample, the peak shape is
36 attributed to the presence of (at least) two species. The main species (indicated with "M" in
37 the inset; also dominating the spectrum of the as-deposited EVAP- $Cu_2ZnGeSe_4$ sample) is
38 ascribed to a selenide, i.e., to selenium in a $Cu_2ZnGeSe_4$ and/or ZnSe environment – based

1 on the comparison of the Se 3d data with Ref. [12]. Based on this data it is not possible to
2 unambiguously differentiate between ZnSe and $\text{Cu}_2\text{ZnGeSe}_4$. The low-intensity secondary
3 species (indicated with “S” in the inset) that is responsible for the additional high-binding
4 energy spectral intensity can most likely be explained by oxidized selenium (SeO_x , $x \geq 3$).
5 However, note that due to the large spread of binding energy values found in published
6 references [12], the presence of a germanium selenide binary phase (with Ge being in an
7 oxidation state $> 2+$) and/or formation of Se-C bonds (in-line with the increased C signal) can
8 also not be ruled out as an explanation for the high-binding energy Se 3d contribution.
9 Whether and how this second Se species affects the chemical environment of additional
10 $\text{Cu}_2\text{ZnGeSe}_4$ elements and/or the electronic structure of the absorber and how this is related
11 to the observed solar cell characteristics is the topic of ongoing research. Work on the device
12 level is in progress with the goal of developing a wet-chemical treatment to remove the HCl-
13 etch induced formation of the second Se species in order to recover the FF and collection
14 length, while keeping the V_{OC} gain resulting from HCl etching.

15 2.2.2. BUFFER LAYER DEVELOPMENT

16 The most widely used buffer layer for Cu chalcogenide thin film solar cells is CdS prepared
17 by CBD. This preparation process results in a highly defect-rich material, also containing
18 oxygen (OH) and carbon impurities [28]. Some of the properties of CBD-grown CdS (e.g.
19 composition, defect nature, structure) depend on the experimental deposition parameters
20 (concentration of the precursors, temperature of the chemical bath, etc.). Consequently, the
21 CBD-CdS recipe needs to be adjusted for each absorber material for optimal solar cell
22 performance. Hence, we empirically tuned the experimental parameters of the CdS
23 deposition on the evaporated EVAP- $\text{Cu}_2\text{ZnGeSe}_4$ absorbers. We observe a V_{OC} increase with
24 increasing deposition duration, accompanied with a decrease of FF and J_{SC} after a critical
25 duration. More details about the buffer layer optimization, which resulted in a new record
26 efficiency of 7.6 % for $\text{Cu}_2\text{ZnGeSe}_4$ based solar cells, can be found in Ref. [29].

27 Although it is the most-used buffer material for kesterite solar cells, CdS has a quite low
28 optical band gap energy (2.4 eV) and high absorption coefficient for a material that would
29 ideally be transparent. Consequently, there is a loss in current due to absorption of solar
30 radiation in the CdS is in the range of 1-2 mA/cm². In case of a potential kesterite/Si tandem
31 configuration, this loss would manifest in a 4 to 14 % relative decrease of the theoretically
32 achievable J_{SC} [3]. Moreover, another important prerequisite to reach high efficiency is an ideal
33 buffer/absorber interface that allows for lossless charge carrier transport without barriers for
34 charge carriers and preventing high-rate charge carrier recombination routes. In order to
35 systematically optimize the buffer/kesterite interface, we prepared solar cells based on wet-
36 chemical deposited (see Section 2.1.2) 1.5 (+/- 0.05) eV band gap SOL- $\text{Cu}_2\text{ZnGe}(\text{S},\text{Se})_4$
37 absorbers (prepared according to the solution approach discussed in detail in Section 2.1.2)

1 and different buffer layer materials. The five different buffer materials used were: sputtered
2 (“rf”) $\text{Zn}(\text{O}_{0.6}\text{S}_{0.4})$, CBD- $\text{Zn}(\text{O},\text{S})$, CBD- CdS , atomic layer chemical vapor deposited (ALCVD)
3 In_2S_3 , and co-evaporated (“co-evap.”) CdIn_2S_4 . A detailed discussion can be found in Ref. [17],
4 briefly: Compared to the CdS reference, In_2S_3 and $\text{Zn}(\text{O}_{0.6}\text{S}_{0.4})$ buffers have a higher
5 transmission, i.e., less absorption in the buffer layer (in the 350-500 nm wavelength range), as
6 shown in Figure II. Solar cells with $\text{Zn}(\text{O}_{0.6}\text{S}_{0.4})$ buffers also yield higher V_{OC} values. For these
7 devices, a higher activation energy of the dominant recombination process was also derived
8 (compared to the CdS reference) [17], strongly suggesting a more preferable electronic
9 structure of the buffer/SOL- $\text{Cu}_2\text{ZnGe}(\text{S},\text{Se})_4$ interface. The sputtered- $\text{Zn}(\text{O}_{0.6}\text{S}_{0.4})$ buffered
10 solar cells, however, achieve a lower overall efficiency, mainly due to reduced FF and J_{SC} , as
11 presented in Table SI [17]. We speculate that those losses originate from the nature of the
12 deposition method, as all vacuum deposited buffer layers suffer from similar J_{SC} and FF losses,
13 compared to solution-prepared CdS . For that reason, we also investigated wet-chemically
14 deposited $\text{Zn}(\text{O},\text{S})$ buffers. With CBD- $\text{Zn}(\text{O},\text{S})$ buffers, SOL- $\text{Cu}_2\text{ZnGe}(\text{S},\text{Se})_4$ based solar cells
15 achieve similar FF and J_{SC} values as the CdS reference, but lower V_{OC} values. A tentative
16 explanation for this observation is the different composition of CBD- $\text{Zn}(\text{O},\text{S})$ and sputtered-
17 $\text{Zn}(\text{O}_{0.6}\text{S}_{0.4})$ buffers: certainly the O/S ratio, which determines the optical band gap of the
18 $\text{Zn}(\text{O},\text{S})$ material, can be different and the CBD- $\text{Zn}(\text{O},\text{S})$ buffer may also contain oxide,
19 hydroxide (OH), and/or carbon impurities, which can also have an impact on the
20 optoelectronic properties. Additional work is in progress to optimize the CBD- $\text{Zn}(\text{O},\text{S})$ buffer
21 aiming at combining the good J_{SC} and FF values with the high V_{OC} that is obtained when
22 sputtered- $\text{Zn}(\text{O}_{0.6}\text{S}_{0.4})$ is used as a buffer.

23

24 2.3.DEVICE SIMULATIONS

25 Numerical simulations were carried out using the SCAPS software [30] to determine the best
26 device design for $\text{Cu}_2\text{ZnGe}(\text{S},\text{Se})_4$ -based top cells in a tandem configuration, with a focus on
27 suggesting suitable TBCs. The parameters used in the simulations are listed in Table S2
28 [31,32]. Most of the parameters related to the absorber material, such as thickness, doping
29 concentration, band gap, and absorption coefficient, were extracted from (our own) electrical
30 and optical measurements. Parameters related to MoSe_2 and MoO_3 were taken from
31 literature, and those related to CdS and ZnO:Al layers are already available in the SCAPS
32 software. Two configurations were tested in the simulations: $\text{Cu}_2\text{ZnGe}(\text{S},\text{Se})_4$ substrate or
33 superstrate solar cells, as shown in Figure S5. In the standard configuration [substrate, Figure
34 S5(a)], a thin layer of MoSe_2 was inserted in the model between the $\text{Cu}_2\text{ZnGe}(\text{S},\text{Se})_4$ absorber
35 layer and the Mo contact. The presence of MoSe_2 layer at the absorber/Mo interface was
36 previously reported for $\text{Cu}(\text{In},\text{Ga})\text{Se}_2$ [33] and $\text{Cu}_2\text{ZnSnSe}_4$ [34] TF solar cells. It was shown
37 to be beneficial for TF solar cells performance if its thickness is controlled to avoid detrimental

1 effects on series resistance. The improvement of the solar cell performance is mainly due to
2 a reduction of the barrier height and better charge carrier collection at the interface between
3 the absorber and the Mo contact if MoSe₂ is present. For tandem cells, the Mo back contact
4 needs to be replaced by a TBC, see Figure S5(b). However, most of the transparent
5 conductive oxides (TCOs) used in solar cells have a low work function (4.7-4.9 eV [35]) and
6 thus – if Anderson’s rule holds true for these complex heterojunctions – may not result in a
7 preferable energy level alignment with the Cu₂ZnGe(S,Se)₄ absorber layer when used as back
8 contact. In this case, the use of an intermediate layer, such as a thin MoSe₂ or MoO₃, can
9 mitigate this issue. MoO_x was successfully used in superstrate configuration as an interfacial
10 layer between a transparent SnO₂:In (ITO) back contact and Cu(In,Ga)Se₂ absorbers [36] and
11 was shown to also be a good interfacial layer for the Cu₂ZnSnSe₄ based solar cells (applied
12 either as a layer between the absorber and the Mo contact to improve the back contact
13 properties or as a primary back contact) [37-38].

14 Figure S6 shows the J(V) curves calculated for different device configurations. The solar cell
15 parameters are given in Table 2. For the Cu₂ZnGe(S,Se)₄ substrate configuration (a), the
16 calculated J(V) curve is based on series resistance and shunt resistance values of 4.7 and
17 365 Ωcm², respectively. These resistances have been extracted from the J(V) curve of one of
18 the most efficient EVAP-Cu₂ZnGeSe₄ substrate solar cells (5.4 % power conversion efficiency).
19 In the configurations (b)-(d), the J(V) curves were calculated after the (simulated) optimization
20 of the absorber doping concentration (10¹⁶ cm⁻³) and of the values for series and shunt
21 resistance (R_s ≤ 0.5 Ωcm²; R_{sh} ≥ 800 Ωcm²). In case of a superstrate with TBC [configuration
22 (c)], the low solar cell performance is due to a strong reduction of the V_{OC} caused by the low
23 work function of ZnO:Al (AZO). The best configuration for superstrate solar cell was
24 obtained by considering a thin “buffer layer” of MoO₃ between the absorber and a TCO back
25 contact (d). It should be noticed that an ITO back contact acts also as a Na barrier. If
26 insufficient Na content limits the device performance, however, Na needs to be deliberately
27 added in a controlled way, e.g. by means of post-deposition treatment [39].

29 2.4. TRANSPARENT BACK CONTACTS

30 TBCs for potential use in the wide band gap Cu₂ZnGe(S,Se)₄ kesterite top cell of a four
31 terminal photovoltaic tandem cell with a c-Si bottom cell have been studied. In addition to
32 the electronic structure considerations in the previous section, the back contact must be
33 transparent for photons with an energy below the band gap of the absorber layer and stable
34 under its processing conditions. Independent of the processing route [evaporation-based (see
35 Section 2.1.1) or solution-based (see Section 2.1.2.)], the kesterite absorber is formed by high-
36 temperature annealing of the precursor layer stack in H₂Se and/or H₂S atmosphere. It is
37 expected that this selenization/sulfurization will be the most critical processing step that the

1 TBC has to withstand. H_2Se is a more powerful reducing agent than is H_2S [40], and so we
2 focus on the impact of annealing in H_2Se atmosphere on the optoelectronic and chemical
3 properties of the TBCs in the following. The most widely used TCOs: ITO, AZO, and $SnO_2:F$
4 (FTO) – were selected for exposure tests [41,42]. It is assumed that the S-containing
5 atmosphere during annealing required to achieve the $[S]/([S]+[Se])$ composition necessary for
6 the desired higher absorber band gap will have similar effects.

7 In order to simulate the impact of H_2Se exposure during a $Cu_2ZnGe(S,Se)_4$ deposition process,
8 the optical and chemical properties of the selected TCOs have been tested before and after
9 exposure to a 20 sccm H_2Se flow for 15 min at various treatment temperatures (400 and
10 450 °C). A first screening showed that ITO had the highest likelihood for yielding working
11 devices but would require a protective top layer (to make it more stable during absorber
12 processing). Furthermore, our SCAPS simulations (see Section 2.3) of $Cu_2ZnSn(S,Se)_4$ devices
13 had shown that employing ITO instead of Mo (which is the standard back contact for single-
14 junction devices) would result in an efficiency drop of 60 rel.% (see Table 2). The same
15 simulations showed that this deterioration may be fully prevented by using an additional MoO_3
16 interlayer between ITO and absorber resulting even in an efficiency gain of 80 rel.% (see Table
17 2). Hence, thin sputtered MoO_3 layers applied on top of a 135-nm-thick sputtered ITO before
18 absorber deposition – as protection layer and for improved energy level alignment – were
19 first explored. However, MoO_3 is significantly reduced upon H_2Se exposure; in Section 2.4.1,
20 we explore alternative protective layers.

21 2.4.1. PROTECTIVE TOP LAYERS

22 In this section, the effectiveness of Al_2O_3 , $InZnO_x$ (IZO), and TiO_2 as protection of ITO during
23 selenization/sulfurization is explored. The study is conducted by means of H_2Se exposure tests
24 at 400°C and 450°C (i.e., annealing temperatures relevant for absorber formation), as well as
25 by experiments on the device level. The top layers were deposited by means of atmospheric
26 pressure spatial atomic layer deposition (S-ALD, plasma enhanced for IZO) [43].

27 2.4.1.1. LAYER PROPERTIES

28 Al_2O_3 is known to be an excellent passivation and barrier (i.e., protective layer) material of
29 high chemical stability; it is however electrically insulating. IZO and TiO_2 are candidates for
30 forming more conductive protective layers. In order to determine the minimum thickness for
31 being a sufficient protective top layer and to test if such a thickness would yield a working
32 device, a set of Al_2O_3 (1-30 nm), IZO (1-120 nm), and TiO_2 (2-60 nm) layers of different
33 thicknesses were deposited by means of S-ALD on ITO coated SLG substrates. The
34 absorption spectra (derived from reflectance and transmittance) shown in Figure 12 suggest
35 that the decrease of ITO transmittance (i.e., increase of absorption) induced by H_2Se exposure
36 could (to some degree) be prevented with a > 2 nm Al_2O_3 (not shown), > 30 nm IZO, or $>$

1 60 nm TiO₂ top layer. However, the TiO₂ layers are less effective at temperatures of 450°C
2 and higher [see Figure 12(c)]. After H₂Se exposure at 450°C, the average absorption for an
3 135-nm-thick ITO layer with a 30-nm-thick IZO and 60-nm-thick TiO₂ protective layer is 8
4 and 18 %, respectively, in the near infra-red regime (between 750 nm and 1100 nm).

5 HAXPES was used for chemical structure analysis of the IZO/ITO back contact configuration
6 and its changes upon H₂Se exposure in order to probe the deterioration of ITO and the
7 protection mechanism of IZO. Note that same measurement conditions apply as for the
8 HAXPES data shown in Figures 1 and 4. The Sn 3d XPS spectra of a bare ITO sample and ITO
9 samples with either a 10 or a 30 nm protective IZO top layer before and after H₂Se treatment
10 at 450 °C are shown in Figure 13. Before the H₂Se treatment, for the bare ITO and 10 nm
11 IZO/ITO sample, Sn resides in a chemical environment best described by a combination of
12 ITO, SnO, and SnO₂. However, note that asymmetric core level lines are generally found for
13 (highly conductive) ITO and are generally attributed to final-state effects [44]. No Sn signal is
14 observed for the 30 nm IZO/ITO sample, due to insufficient probing depth and complete
15 coverage of the ITO by the IZO. (The inelastic mean free path of the Sn 3d photoelectrons
16 excited with 6 keV photons in In₂O₃ is around 7 nm [45]). After H₂Se treatment, the spectral
17 intensity of the Sn 3d line is significantly redistributed, indicating that the chemical
18 environment of Sn has changed; SnSe and/or SnSeO_x are likely present. Furthermore, the Sn
19 3d intensity increases after the H₂Se treatment for the 10 nm IZO/ITO sample, suggesting
20 either that Sn diffuses into the IZO layer and/or the degree of ITO coverage decreases. If the
21 protective layer does not completely cover the ITO, it will not prevent the chemical reaction
22 between ITO and H₂Se, the evidence of which is the formation of Sn-Se bonds. Additional
23 HAXPES data suggest a significant chemical interaction between IZO and H₂Se, implying that
24 IZO acts as a sacrificial agent to protect ITO from H₂Se. Note that additional measurements
25 on TiO₂/ITO test structures (not shown) reveal a different protection mechanism: TiO₂ is
26 largely unaffected by H₂Se annealing.

27 2.4.1.2. SOLAR CELL DEVICES

28 EVAP-Cu₂ZnGeSe₄-based devices were manufactured on sputtered ITO/SLG substrates with
29 S-ALD deposited Al₂O₃, IZO, and TiO₂ protective layers. As references, similarly prepared
30 devices with a standard Mo back contact on a Si(O,N)/SLG substrate were also fabricated and
31 tested. A CBD-CdS buffer and a sputtered i-ZnO/AZO bi-layer emitter was used as the front
32 window. The (5×5 cm²) EVAP-Cu₂ZnGeSe₄ cell stack samples were finished by applying a
33 Ni/Ag grid for local J(V) measurements. Table 3 depicts measured J(V) parameters of the
34 champion cells. As stated earlier, an Al₂O₃ thickness above 2 nm is needed for an effective
35 H₂Se protection of ITO. However, the 3 nm thick Al₂O₃ layer used here already reduces the
36 cell performance dramatically due to its insufficient conductivity. This issue could be
37 overcome by using a perforated Al₂O₃ layer, which (through the formed point contacts) allows

1 sufficient charge carrier transport while also acting as a passivation and barrier layer. Devices
2 with an ITO back contact with or without either a 30 nm TiO₂ or IZO protective top layer
3 function better, yielding efficiencies of about 85-90 % of that of reference cells with a Mo back
4 electrode. The lower efficiencies likely result from a higher sheet resistance of the back
5 contact and a presumably less ideal energy level alignment at the absorber/back contact
6 interface compared to the Mo back electrode. The combination of ITO back electrode with
7 TiO₂ protection layer results in a higher V_{OC} than an ITO back electrode with or without IZO
8 protection layer, but not in a higher J_{SC} value – finding an explanation for this observation is a
9 subject of ongoing discussion.

10 Figure 14 depicts the absorption (derived from reflectance and transmittance) for a complete
11 EVAP-Cu₂ZnGeSe₄ solar cell layer stack on a 60 nm TiO₂ protected ITO back electrode. The
12 absorption of the complete cell stack for energies directly below E_G (Cu₂ZnGeSe₄) is 65 % for
13 60 nm TiO₂/ITO and 55 % for 30 nm IZO/ITO (not shown) back contacts. These values are
14 higher than the sum computed from the absorption of the individual layers (i.e., back contact
15 after H₂Se exposure, absorber, and front window), as illustrated in Figure 14 for the 60 nm
16 TiO₂/ITO back contact. This may be due to slightly varying absorber layer deposition and/or
17 selenization process conditions, annealing-induced formation of species at the absorber
18 (precursor)/TBC interface, or internal reflections and higher absorption of the front window
19 when deposited on the actual (rough) absorber layer. In order to reduce the optical losses in
20 a complete device, more analysis of the composition and morphology of the layers and their
21 interfaces in the cell stack will be needed. To reduce near-infrared absorption due to free
22 charge carriers in both the highly-doped back and front contact, more effort is required to
23 develop transparent materials with high mobilities and reasonable charge carrier densities.

24

25 3. OUTLOOK

26 The bottom cell in a tandem configuration will only receive the illumination transmitted
27 through the top cell, and so a good transmission at $h\nu <$ than the top cell absorber band gap
28 is crucial for the top cell structure to successfully be employed in tandem configurations, as
29 discussed in the previous section. A thin top cell combined with a TBC is generally used to
30 assure this. To investigate the effect of the top cell transparency on the performance of the
31 bottom cell (c-Si), we calculated the efficiency of the bottom cell as a function of the light
32 transmitted through the top cell, as shown in Figure 15. The bottom cell is modeled as a 25
33 % efficient silicon cell with rear locally diffused contacts (PERL technology [46]) and
34 Lambertian light trapping [47-48]. For the tandem cell, a four-terminal mechanically stacked
35 configuration is considered. In Figure 15, the efficiency of the c-Si bottom cell under the
36 absorbing 1.5 eV band gap Cu₂ZnGe(S,Se)₄-based cell is shown as a function of top cell

1 transmission. Furthermore, the total efficiency of the tandem configuration assuming a top
2 cell efficiency of 8, 15, and 22 % is shown. In the case of a $\text{Cu}_2\text{ZnGe}(\text{S},\text{Se})_4$ (1.5 eV)-based top
3 cell of 8 % efficiency (i.e., a performance level similar to the one reached as a result of joint
4 research efforts of this consortium, see Section 2.2.2), a transparency higher than 80 % is
5 required to achieve a total tandem device efficiency that is higher than the efficiency of the c-
6 Si bottom cell alone (25 %, horizontal dashed line in Fig. 21). In case the efficiency of the top
7 cell can be increased to 15 % (a performance level that seems feasible based on our device
8 simulation in Section 2.3, see Table 2), a transparency above 50 % is sufficient for viable
9 tandem application. Finally, for a 22 % efficient top cell (a performance level that has been
10 shown for other polycrystalline chalcogenide-based absorbers [2]) respective tandem devices
11 would reach efficiencies > 25% with even more relaxed top cell transparency requirements.

12 A maximal transparency of approximately 40 % for a real-world $\text{Cu}_2\text{ZnGe}(\text{S},\text{Se})_4$ /TBC layer
13 stack was shown in this contribution (see Fig. 20 and discussion in Section 2.4.1.2); there is a
14 realistic potential to increase this to 60 % if chemical reactions at the interfaces and/or internal
15 reflections can be minimized. Hence, wide band gap kesterites might very well represent a
16 material class that may be used as absorber in tandem device top cells if further significant
17 advancements in cell performance (8 → 15%) and transmission (40 → 60%) are achieved.
18 Based on the progress presented in this paper (compare status 2015 and 2018 indicated as
19 ❶ and ❷ in Figure 15), it indeed seems feasible to reach the realistic performance scenario
20 (❸ in Figure 15) if optimization efforts continue.

21

22 4. CONCLUSIONS

23 Absorbers in which Sn had been substituted by Si did not result in functioning solar cells; most
24 likely due to too high doping (in the order of 10^{18} cm^{-3}) and/or the formation of SiO_2 at the
25 absorber surface. However, $\text{Cu}_2\text{ZnGe}(\text{S},\text{Se})_4$ absorbers with band gaps above 1.5 eV have
26 been successfully developed and integrated into solar cells. Typically, ZnSe is present in large
27 amounts on the top surface of these absorbers; it is shown here that this impurity can be
28 selectively removed with chemical etching: (i) with 12 wt% HCl at a temperature of 60-85 °C,
29 and (ii) in 1M KMnO_4 / 1M H_2SO_4 aqueous solution. The standard CBD-CdS has been
30 optimized, resulting in a record efficiency of 7.6 % for EVAP- $\text{Cu}_2\text{ZnGeSe}_4$ based solar cells
31 (with Mo back contact). In_2S_3 , $\text{Zn}(\text{O},\text{S})$, and CdIn_2S_4 alternative buffer layers were also tested,
32 where the highest V_{OC} and presumably the best electronic buffer/absorber interface structure
33 could be obtained with sputtered $\text{Zn}(\text{O},\text{S})$.

34 The solar cell performance of substrate/superstrate $\text{Cu}_2\text{ZnGe}(\text{S},\text{Se})_4$ solar cells with TBC for
35 tandem application was simulated using SCAPS to evaluate various configurations and identify
36 performance-limiting factors. It was found that when low work function, TCO-based, TBCs

1 (like ITO) are used, an “interlayer” is required to reduce the blocking barrier at the
2 absorber/TCO interface, ideally achieving an Ohmic contact. The device simulation suggests
3 MoO_x as an ideal interlayer candidate material for $\text{Cu}_2\text{ZnGe}(\text{S},\text{Se})_4$ superstrate cells for
4 tandem applications. MoO_x is, however, unstable under real-world absorber processing
5 conditions; the use of an alternative, stable material causes the majority of respective
6 (transparent) cells to be still limited by a low V_{OC} .

7 ITO was shown to be a well-performing candidate for a TBC, but it requires a protective top
8 layer (i.e., Al_2O_3 , IZO, or TiO_2) if it is to remain transparent after exposure to the Se (and/or
9 S) atmosphere needed for the absorber deposition process. ITO back contacts with a
10 protective layer of 30-nm-thick IZO or 60-nm-thick TiO_2 have an average absorption of 8 and
11 18 %, respectively, in the near infra-red regime. The efficiency of solar cells using an ITO with
12 IZO or TiO_2 protective layers achieves 85-90 % of the performance of reference cells with
13 Mo back contact (at a maximal transparency of 40 %).

14 In summary, $\text{Cu}_2\text{ZnGe}(\text{S},\text{Se})_4$ absorbers with potential for future application as top cell in
15 tandem configurations have been developed. Different optimization routes mostly addressing
16 the buffer/absorber interface have been suggested and proven to be effective to advance
17 device performance. In order to make wide band gap kesterites a prime candidate absorber
18 material for the top cell in tandem devices, similar approaches are crucially needed extending
19 the efforts to all aspects of the complete cell stack, tackling interface *and* bulk properties in
20 order to improve cell efficiency and transmission. In order to accomplish this challenge, it is
21 proposed to focus future research on increasing the solar cell performance before addressing
22 the transparency of these solar cell devices.

1 ACKNOWLEDGEMENTS

2 This project has received funding from the European Union's Horizon 2020 research and
3 innovation program under grant agreement N° 640868. The synchrotron radiation
4 experiments were performed at the SPring-8 beamline BL15XU with the approval of the NIMS
5 Synchrotron X-ray Station (Proposals 2016A4600, 2016B4601, and 2017A4600) and at BESSY
6 II with the approval of HZB. B. Vermang has received funding from the European Research
7 Council (ERC) under the European Union's Horizon 2020 research and innovation
8 programme (grant agreement n° 715027).

9

10

11 REFERENCES

12 [1] M.A. Green, S. Hishikawa, E.D. Dunlop, D.H. Levi, J. Hohl-Ebinger, A.W.Y. Ho-Baillie,
13 Prog. Photovoltaics Res. Appl., 2018, **26**, 3-12.

14 [2] Solar Frontier Achieves World Record Thin-Film Solar Cell Efficiency of 22.9 %, Solar
15 Frontier press release, http://www.solar-frontier.com/eng/news/2017/1220_press.html, last
16 accessed May 23rd 2018.

17 [3] W. Shockley, H.J. Queisser, J. Appl. Phys., 1961, **32**, 510-519.

18 [4] T.P. White, N.N. Lal, K.R. Catchpole, IEEE J. Photovoltaics, 2014, **4**, 208-214.

19 [5] T.K. Todorov, D.M. Bishop, Y. Seog Lee, Sol. Energy Mater. Sol. Cells, 2018, **180**, 350-
20 357.

21 [6] S. Siebentritt, S. Schorr, Prog. Photovoltaics Res. Appl., 2012, **20**, 512-519.

22 [7] W. Wang, M.T. Winkler, O. Gunawan, T. Gokmen, T.K. Todorov, Y. Zhu, D.B. Mitzi,
23 Adv. Energy Mater., 2014, **4**, 1301465.

24 [8] M. León, S. Levchenko, R. Serna, G. Gurieva, A. Nateprov, J.M. Merino, E. J. Friedrich, U.
25 Fillat, S. Schorr, E. Arushanov, J. Appl. Phys., 2010, **108**, 093502.

26 [9] Q. Shu, J.-H. Yang, S. Chen, B. Huang, H. Xiang, X.-G. Gong, S.-H. Wei, Phys. Rev. B,
27 2013, **87**, 115208.

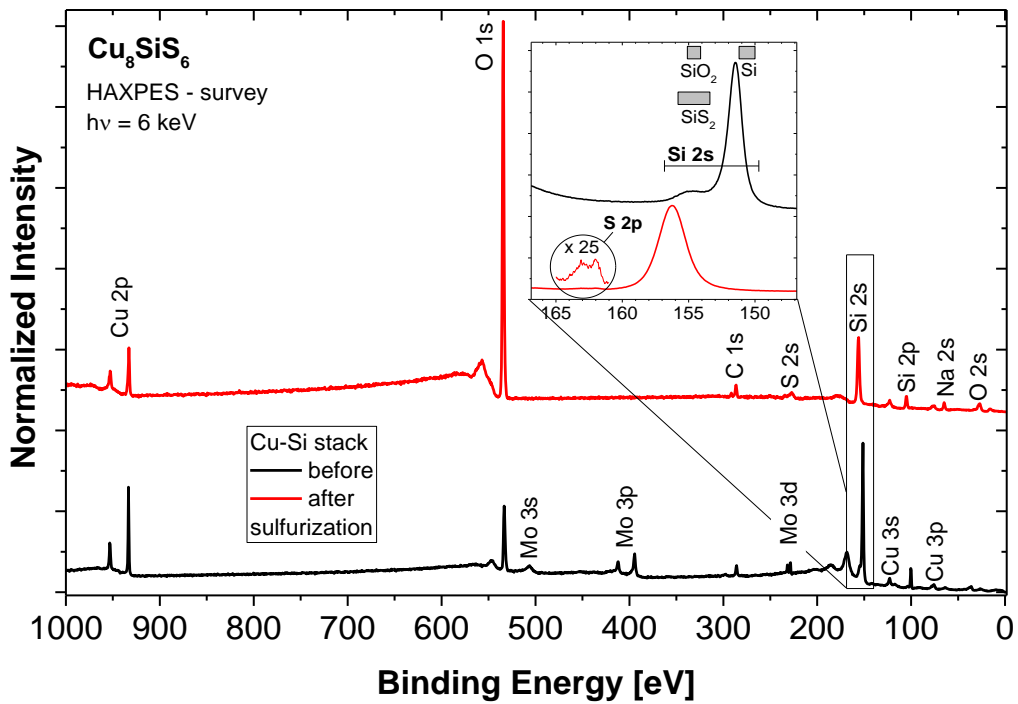
28 [10] G. Brammertz, B. Vermang, H. Elanzeery, S. Sahayaraj, S. Ranjbar, M. Meuris, J.
29 Poortmans, Thin Solid Films, 2016, **616**, 649-654.

30 [11] G. Brammertz, B. Vermang, H. Elanzeery, S. Sahayaraj, S. Ranjbar, M. Meuris, J.
31 Poortmans, Phys. Status Solidi C, 2017, **14**, 1600162.

- 1 [12] NIST X-ray Photoelectron Spectroscopy Database, version 3.5, National Institute of
2 Standards and Technology, Gaithersburg, 2003, <https://srdata.nist.gov/xps/>, last accessed
3 May 23rd 2018.
- 4 [13] G. Brammertz, B. Vermang, M. Meuris, J. Poortmans, *Thin Solid Films*, 2019, **670**, 76-
5 79.
- 6 [14] T. Schnabel, M. Seboui, E. Ahlswede, *RSC Adv.*, 2016, **7**, 26-30.
- 7 [15] S. Ueda, Y. Katsuya, M. Tanaka, H. Yoshikawa, Y. Yamashita, S. Ishimaru, Y. Matsushita,
8 K. Kobayashi, *AIP Conference Proceedings*, 2010, **1234**, 403-406.
- 9 [16] S. Ueda, *J. Electron Spectrosc. Relat. Phenom.*, 2013, **190 Part B**, 235-241.
- 10 [17] T. Schnabel, M. Seboui, L. Choubrac, L. Arzel, S. Harel, N. Barreau, E. Ahlswede, *RSC*
11 *Adv.*, 2017, **7**, 40105-40110.
- 12 [18] M. Werner, D. Keller, S.G. Haass, C. Gretener, B. Bissig, P. Fuchs, F. La Mattina, R.
13 Erni, Y.E. Romanyuk, A.N. Tiwari, *ACS Appl. Mater. Interfaces*, 2015, **7**, 12141-12146.
- 14 [19] T. Gershon, K. Sardashti, O. Gunawan, R. Mankad, S. Singh, Y.S. Lee, J.A. Ott, A.
15 Kummel, R. Haight, *Adv. Energy Mater.*, 2016, **6**, 1601182.
- 16 [20] J. Ge, Y. Yu, Y. Yan, *ACS Energy Lett.*, 2016, **1**, 583-588.
- 17 [21] Y. Zhang, J.R.G. Evans, S. Yang, *Journal of Chemical & Engineering Data*, 2011, **56**, 328-
18 337.
- 19 [22] T. Schnabel, M. Seboui, E. Ahlswede, *Energies*, 2017, **10**, 1813.
- 20 [23] J. Chen, W. Li, C. Yan, S. Huang, X. Hao, *J. Alloys Compd.*, 2015, **621**, 154-161.
- 21 [24] M. Kumar, A. Dubey, N. Adhikari, S. Venkatesan, and Q. Qiao, *Energy Environ. Sci.*,
22 2015, **8**, 3134-3159.
- 23 [25] E.M. Gavrishchuk, E.Y. Vilkova, O.V. Timofeev, U.P. Borovskikh, E.L. Tikhonova, *Inorg.*
24 *Mater.*, 2007, **43**, 579-583.
- 25 [26] S. López-Marino, Y. Sánchez, M. Placidi, A. Fairbrother, M. Espindola-Rodríguez, X.
26 Fontané, V. Izquierdo-Roca, J. López-García, L. Calvo-Barrio, A. Pérez-Rodríguez, E.
27 Saucedo, *Chemistry: A European Journal*, 2013, **19**, 14814-14822.
- 28 [27] S. Bourdais, C. Choné, B. Delatouche, A. Jacob, G. Larramona, C. Moisan, A. Lafond, F.
29 Donatini, G. Rey, S. Siebentritt, A. Walsh, G. Dennler, *Adv. Energy Mater.*, 2016, **6**,
30 1502276.
- 31 [28] P. O'Brien, J. McAleese, *J. Mater. Chem.*, 1998, **8**, 2309-2314.

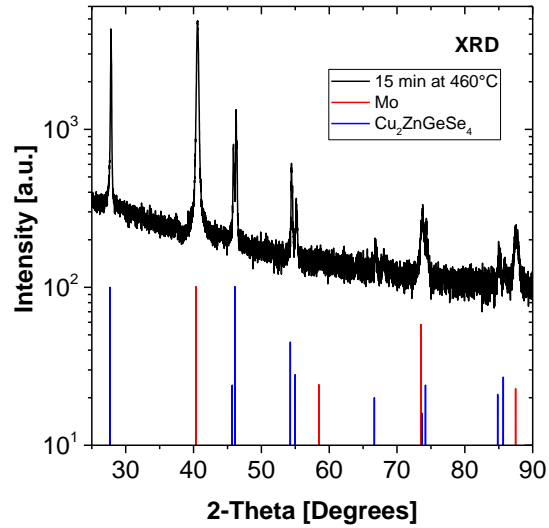
- 1 [29] L. Choubrac, G. Brammertz, N. Barreau, L. Arzel, S. Harel, M. Meuris, B. Vermang,
2 Phys. Status Solidi A, 2018, **215**, 1800043.
- 3 [30] M. Burgelman, K. Decock, S. Khelifi, A. Abass, Thin Solid Films, 2013, **535**, 296-301.
- 4 [31] A. Jäger-Waldau, M.Ch. Lux-Steiner, R. Jäger-Waldau, E. Bucher, Springer Proceedings
5 in Physics, Polycrystalline Semiconductors II, 1991, **54**, 397-402.
- 6 [32] H. Simchi, B.E. McCandless, T. Meng, J.H. Boyle, W.N. Shafarman, J. Appl. Phys., 2013,
7 **114**, 013503.
- 8 [33] D. Abou-Ras, G. Kostorz, D. Bremaud, M. Kälin, F.V. Kurdesau, A.N. Tiwari, M.
9 Döbeli, Thin Solid Films, 2005, **480-481**, 433-438.
- 10 [34] B. Shin, Y. Zhu, N.A. Bojarczuk, S. J. Chey, S. Guha, Appl. Phys. Lett., 2012, **101**,
11 053903.
- 12 [35] A. Klein, C. Körber, A. Wachau, F. Säuberlich, Y. Gassenbauer, S.P. Harvey, D.E. Proffit,
13 T.O. Mason, Materials, 2010, **3**, 4892-4914.
- 14 [36] H. Simchi, J.K. Larsen, K. Kim, W. Shafarman, IEEE J. Photovoltaics, 2014, **4**, 1630-1635.
- 15 [37] S. Lopez-Marino, M. Espindola-Rodriguez, Y. Sanchez, X. Alobé, F. Olivia, H. Xie, M.
16 Neuschitzer, S. Giraldo, M. Placidi, R. Caballero, V. Izquierdo-Roca, A. Pérez-Rodriguez, E.
17 Saucedo, Nano Energy, 2016, **26**, 708-721.
- 18 [38] J. Park, J. Huang, K. Sun, Z. Ouyang, F. Liu, C. Yan, H. Sun, A. Pu, M. Green, X. Hao,
19 Thin Solid Films, 2018, **648**, 39-45.
- 20 [39] D. Rudmann, A.F.d. Cunha, M. Kaelin, F. Kurdesau, H. Zogg, A.N. Tiwari, G. Bilger,
21 Appl. Phys. Lett., 2004, **84**, 1129-1131.
- 22 [40] S. Oae, J.T. Doi, Heteroat. Chem, 1991, **4**, 531.
- 23 [41] I. Volintiru, A. de Graaf, J. van Deelen, P. Poodt, Thin Solid Films, 2011, **519**, 6258-
24 6263.
- 25 [42] J. van Deelen, A. Illiberi, B. Kniknie, H. Steijvers, A. Lankhorst, P. Simons, Surf. Coat.
26 Technol., 2013, **230**, 239-244.
- 27 [43] P. Poodt, D.C. Cameron, E. Dickey, S.M. George, V. Kuznetsov, G.N. Parsons, F.
28 Roozeboom, G. Sundaram, A. Vermeer, J. Vac. Sci. Technol., A, 2012, **30**, 010802.
- 29 [44] C. Körber, V. Krishnakumar, A. Klein, G. Panaccione, P. Torelli, A. Walsh, J.L.F. Da
30 Silva, S.-H. Wei, R.G. Egdell, D.J. Payne, Phys. Rev. B, 2010, **81**, 165207.

- 1 [45] H. Shinotsuka, S. Tanuma, C.J. Powell, D.R. Penn, Surf. Interface Anal., 2015, **47**, 871-
2 888.
- 3 [46] J. Zhao, A. Wang, P.P. Altermatt, S.R. Wenham, M.A. Green, Sol. Energy Mater. Sol.
4 Cells, 1996, **41-42**, 87-99.
- 5 [47] M.A. Green, Prog. Photovoltaics Res. Appl., 2009, **17**, 183-189.
- 6 [48] S. Khelifi, J. Verschraegen, M. Burgelman, A. Belghachi, Renewable Energy, 2008, **33**,
7 293-298.
- 8
- 9



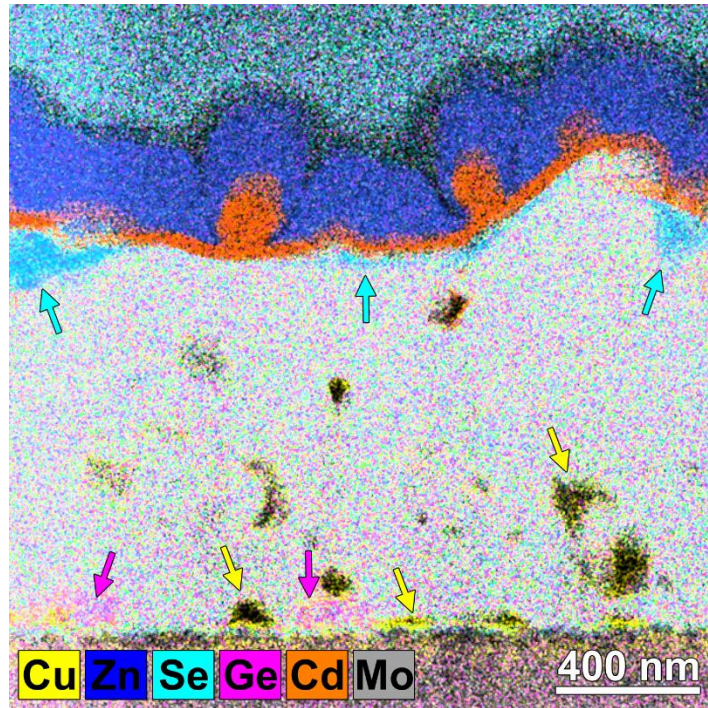
1
 2 Figure 1: Hard x-ray photoelectron survey spectra of an EVAP- Cu_8SiS_6 sample before (black)
 3 and after (red) sulfurization treatment (spectra are offset for clarity). Due to the
 4 sulfurization, the oxygen and sodium (most likely diffused from the soda-lime glass
 5 substrate) contents increase. The inset shows the region of the Si 2s and S 2p core level
 6 lines compared to reference positions [12] of silicon compounds (note that the order of
 7 appearance is different compared to the survey spectra for better visibility). The S 2p line
 8 can only be clearly observed on a magnified (x 25) scale.

9



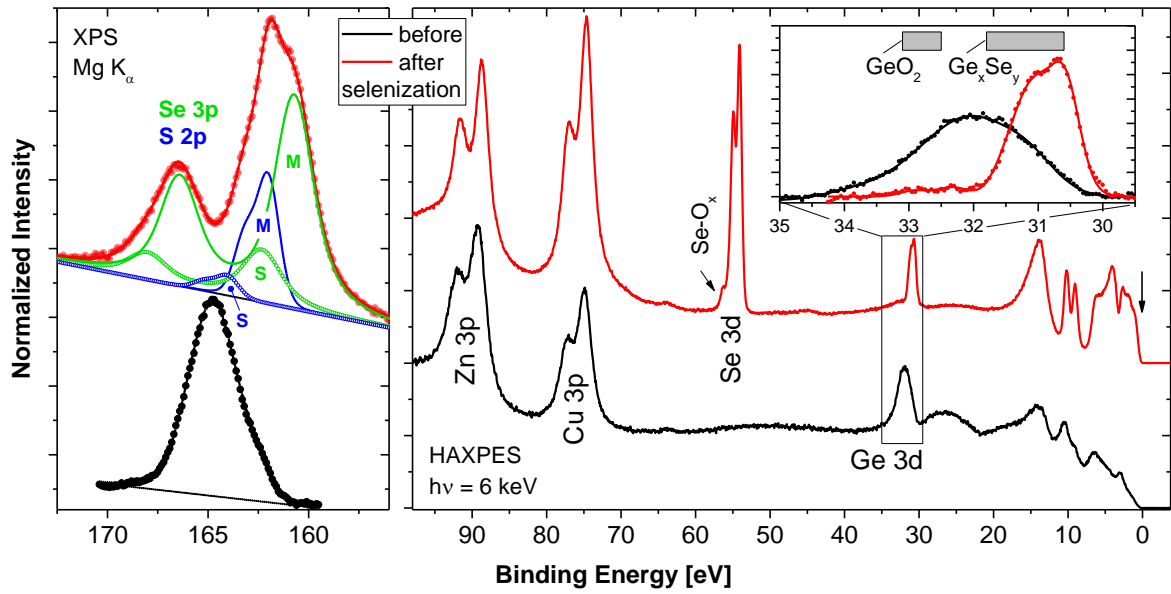
1
2
3
4
5

Figure 2: X-ray diffraction pattern of the EVAP-Cu₂ZnGeSe₄ absorber layer fabricated by selenizing the precursor stack for 15 min at 460°C on a Mo back contact together with reference positions for Cu₂ZnGeSe₄ and Mo (PDF card 00-052-0867).



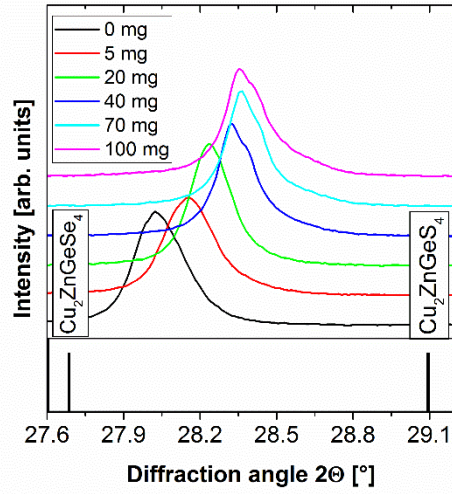
1
2
3
4
5
6
7

Figure 3: Cross-section STEM-EDX elemental map of a complete EVAP-Cu₂ZnGeSe₄ solar cell sample with CdS buffer layer and ZnO window, showing in some regions inhomogeneous elemental distributions, most likely caused by secondary phases. Regions attributed to ZnSe- (blue arrows), Cu₂GeSe₃- (pink arrows), and Cu_{2-x}Se-like (yellow arrows) phases are indicated. See also [13].



1
2
3
4
5
6
7
8
9

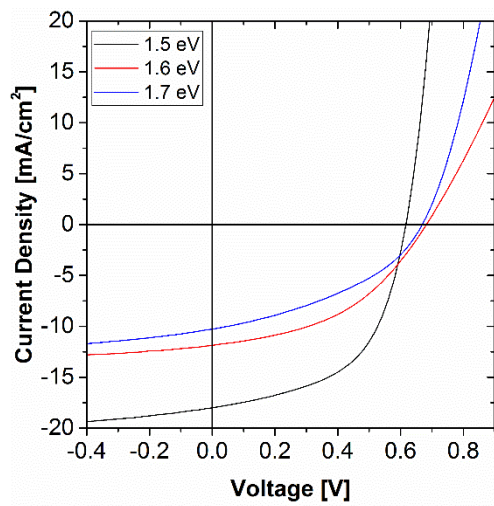
Figure 4: XPS (left panel) and HAXPES (right panel) S 2p/Se 3p and shallow core level spectra, respectively, of a SOL-Cu₂ZnGe(S,Se)₄ absorber before (black) and after (red) Se-annealing induced absorber formation (spectra are offset for clarity). For the S 2p / Se 3p spectrum of the sample after selenization the respective fits of the S 2p (blue) and Se 3p (green) doublets are also shown. (M – main species, S – secondary species). The inset in the right panel shows the region of the Ge 3d shallow core level compared to reference positions for germanium compounds [12].



1

2 Figure 5: 112-reflection of XRD patterns from SOL-Cu₂ZnGe(S,Se)₄ absorbers processed in
3 the presence of different amounts of GeS (0-100 mg).

4



1
2
3
4
5
6

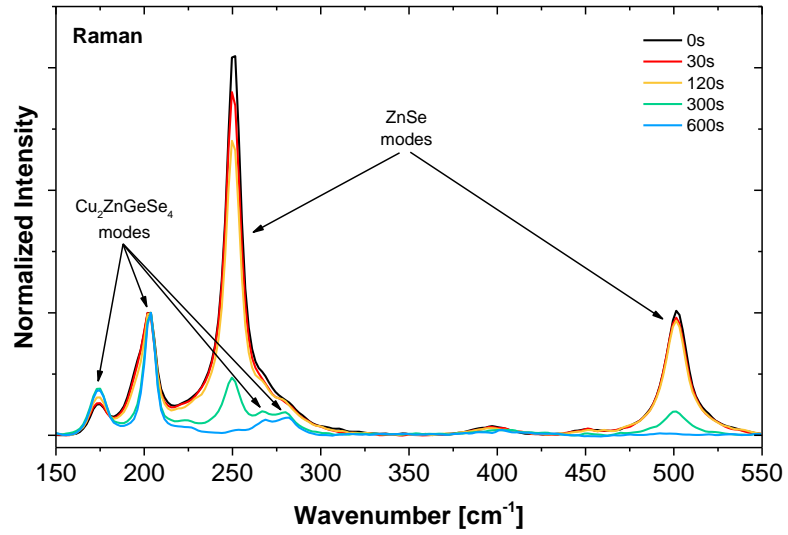
Figure 6: J(V)-characteristics of the best solar cells that were prepared from SOL- $\text{Cu}_2\text{ZnGe}(\text{S},\text{Se})_4$ absorbers with band gaps of 1.5, 1.6, and 1.7 eV, respectively, as determined from EQE. The corresponding $[\text{S}]/([\text{S}]+[\text{Se}])$ -ratios are 0.27, 0.39, and 0.50.

E_G (eV)	1.5	1.6	1.7
Eff. (%)	6.0	3.6	2.7
V_{OC} (mV)	617	683	669
J_{SC} (mA/cm ²)	18.0	11.9	10.3
FF (%)	54.1	44.1	39.7

1

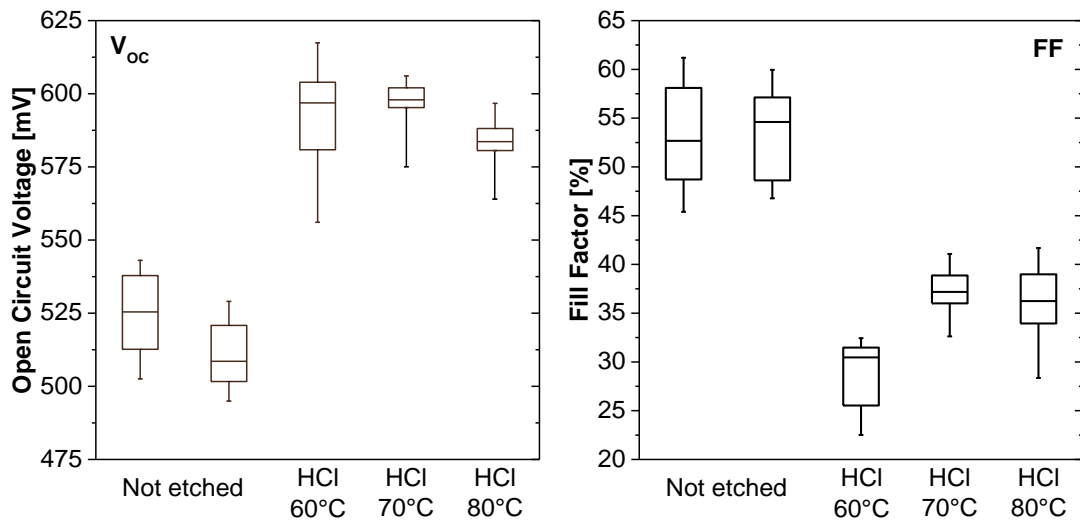
2 Table I: Solar cell parameters of solar cells with SOL-Cu₂ZnGe(S,Se)₄ absorbers with band
3 gaps of 1.5, 1.6, and 1.7 eV, respectively.

4



1
2
3
4
5
6

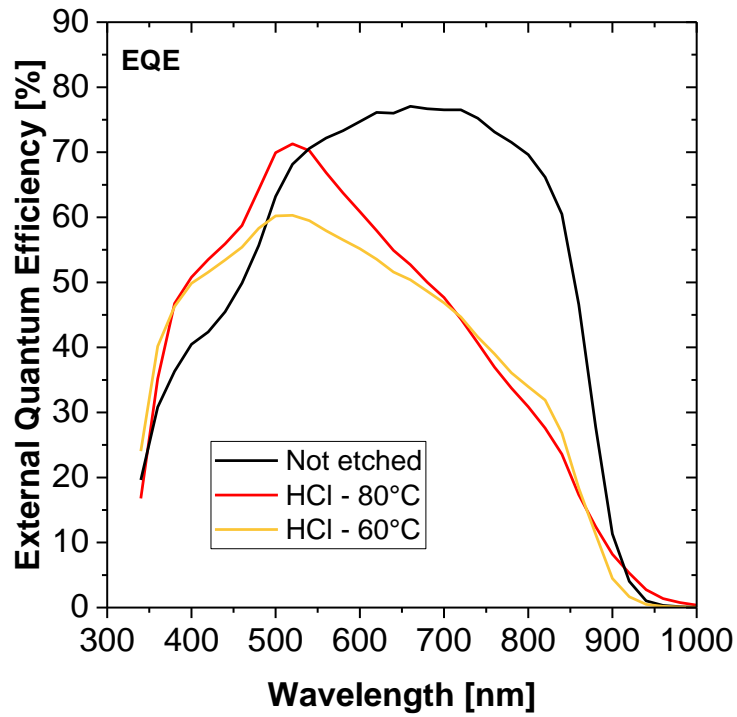
Figure 7: Raman spectra recorded with an excitation wavelength of 458 nm of EVAP-Cu₂ZnGeSe₄ samples that underwent HCl etching (T = 75°C, 12 wt% HCl) for different durations (from 0 to 600 s). Intensities are normalized to the most intense Cu₂ZnGeSe₄ peak (≈ 204 cm⁻¹).



1

2 Figure 8: V_{oc} and FF mean values of EVAP- $Cu_2ZnGeSe_4$ based solar cells prepared using not-
 3 etched absorbers and absorbers HCl etched (using a 12 wt% HCl solution) at different
 4 temperatures (60 min at 60°C, 40 min at 70°C, 15 min at 80°C; 8-12 cells per sample, solar
 5 cell area $\approx 0.5 \text{ cm}^2$).

6

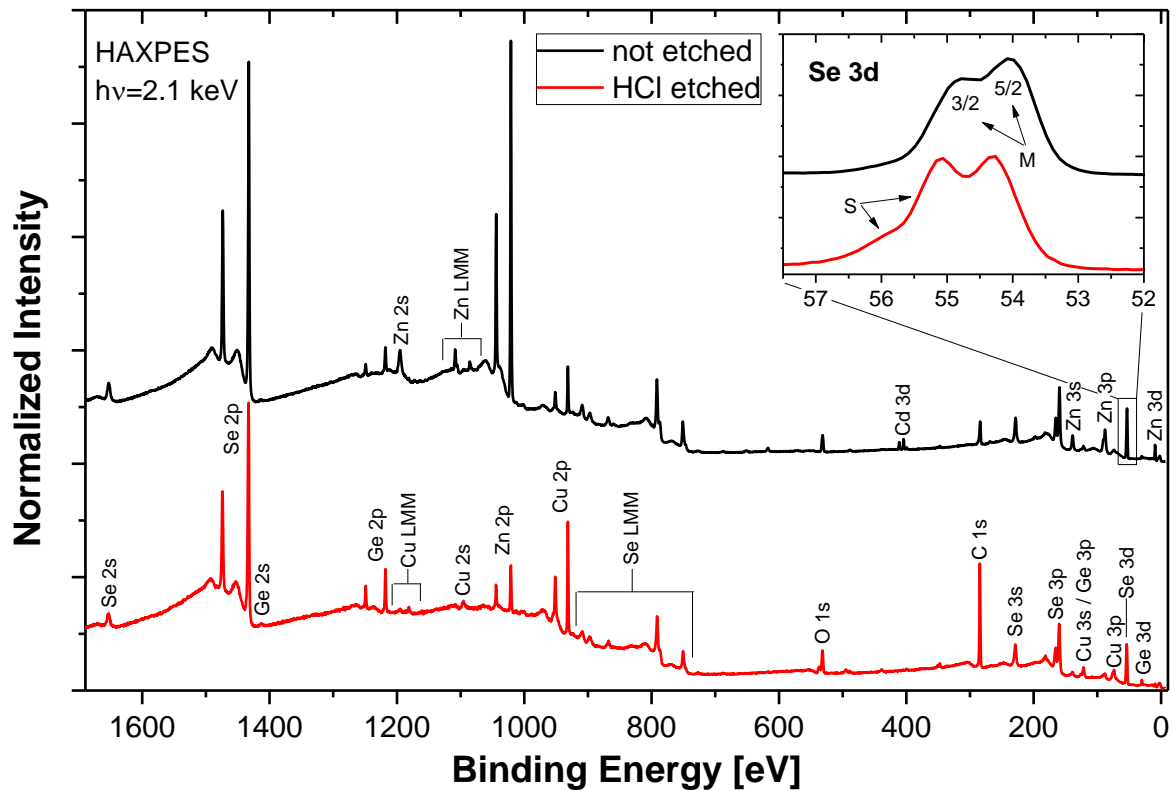


1

2 Figure 9: Representative EQE spectra of EVAP-Cu₂ZnGeSe₄ solar cells based on not-etched
3 absorbers and absorbers HCl etched (using a 12 wt% HCl solution) at different
4 temperatures (60 min at 60°C, 15 min at 80°C).

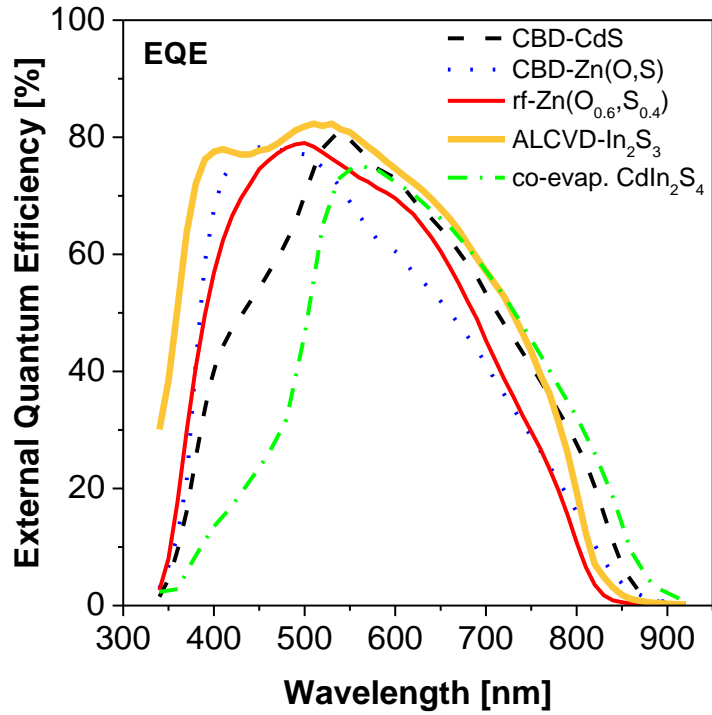
5

6



1
 2 Figure 10: HAXPES survey spectra of an as-deposited / not etched (black spectrum) and
 3 HCl etched (red spectrum) EVAP- $\text{Cu}_2\text{ZnGeSe}_4$ absorber. Spectra are offset for clarity and
 4 all prominent lines are labelled. Inset: Detail spectra of the related Se 3d energy region, with
 5 the 3/2 and 5/2 spin-orbit split doublet indicated. Further, the approximate positions of the
 6 Se $3d_{3/2}$ and $3d_{5/2}$ lines of the main (“M”) and secondary (“S”) selenium species are depicted.

7



1
2
3
4
5

Figure 11: Representative EQE spectra of solar cells with SOL-Cu₂ZnGe(S,Se)₄ absorber and different buffer layers: sputtered (rf) Zn(O_{0.6}S_{0.4}), CBD-Zn(O,S), CBD-CdS, atomic layer chemical vapor deposited (ALCVD) In₂S₃, and co-evaporated (“co-evap.”) CdIn₂S₄.

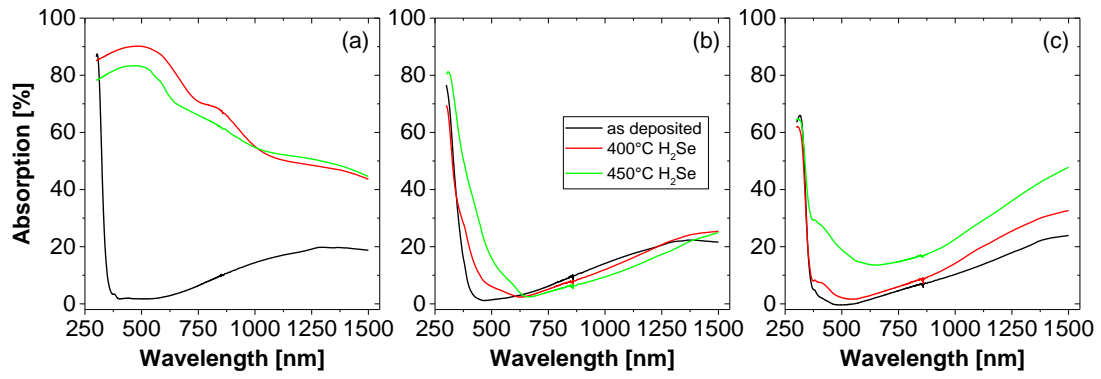
Solar cell parameters	Cell configurations			
	(a)	(b)	(c)	(d)
Back contact	MoSe ₂ /Mo	MoSe ₂ /Mo ^(○)	TCO ^(○)	MoO ₃ /TCO ^(○)
V _{OC} (mV)	553	572	287	1000
J _{SC} (mA/cm ²)	19.70	20.00	17.60	22.00
FF (%)	56.30	71.00	65.54	67.90
Eff. (%)	6.22	8.14	3.31	15.00

1

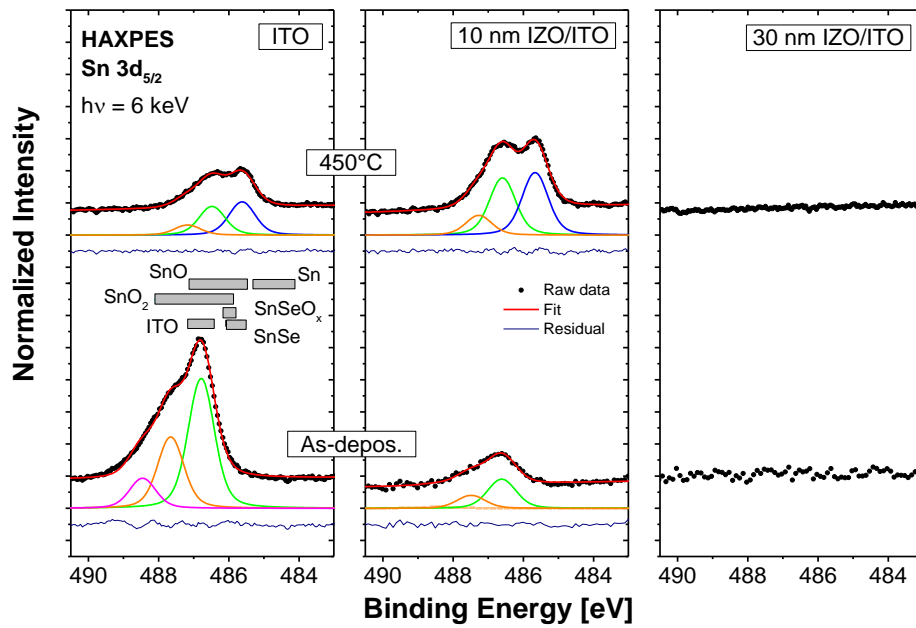
2 Table 2: Solar cell parameters calculated for the different configurations as derived from the
3 J(V) data shown in Figure S6. ^(○) Results from device simulation employing optimized
4 parameters (see Table S2).

5

6



1
 2 Figure 12: Absorption of ITO without (a) and with a 30 nm IZO (b), and with a 60 nm TiO₂
 3 (c) protective top layer before (i.e., as-deposited) and after H₂Se exposure at 400 and
 4 450°C.



1
2
3
4
5
6

Figure 13: Sn $3d_{5/2}$ HAXPES spectra of the ITO, 10 nm, and 30 nm IZO/ITO samples before (“As-depos.”) and after H_2Se treatment at 450 °C. The curve fit was done by using one linear background and three Voigt profiles. The grey boxes indicate the Sn $3d_{5/2}$ energetic position for reference compounds [12].

Back contact	Protective top layer	Eff. _{max} (%)	J _{sc} (mA/cm ²)	V _{oc} (mV)	FF (%)
ITO	None	3.6	19.9	487	37.6
ITO	IZO (30 nm)	4.0	27.1	471	31.2
ITO	Al ₂ O ₃ (3.5 nm)	0.8	9.3	364	23.9
ITO	TiO ₂ (30 nm)	4.3	17.3	600	41.3
SiON/Mo	None	4.7	18.6	600	42.3

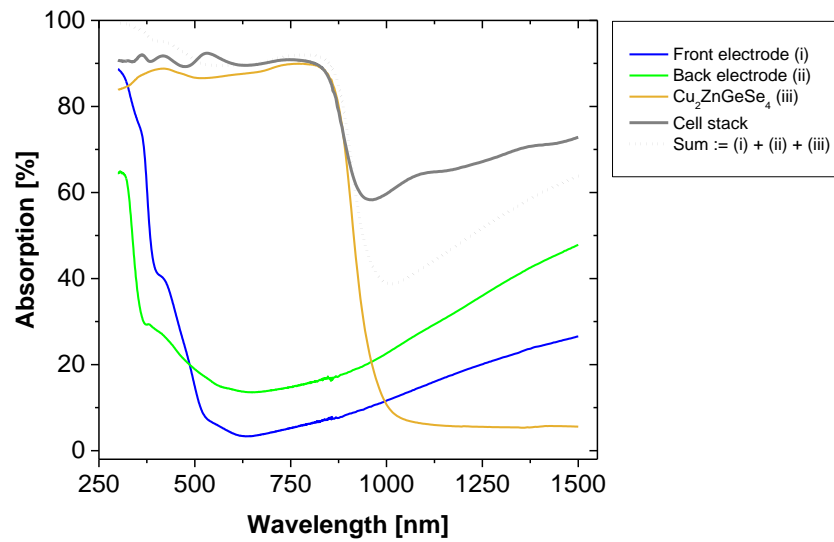
1

2

Table 3: Overview of the J(V) parameters of the manufactured EVAP-Cu₂ZnGeSe₄ devices (best cells).

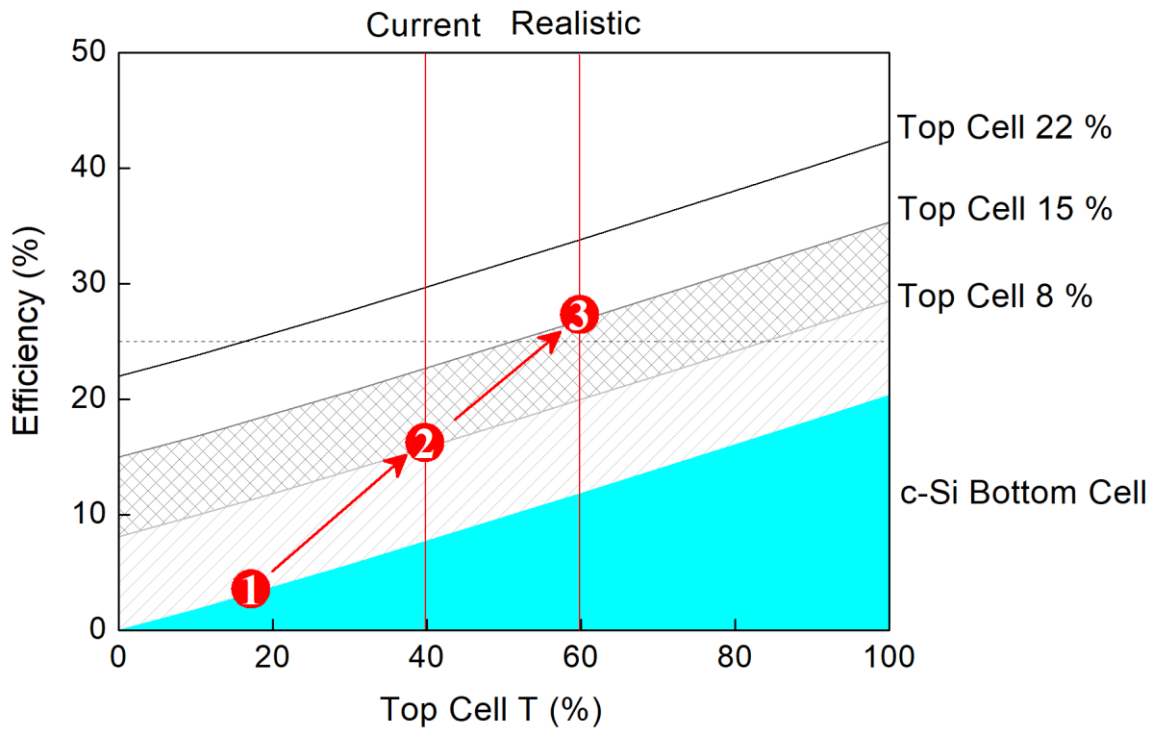
3

4



1
2
3
4
5
6
7

Figure 14: Absorption spectra of the (complete) front electrode/EVAP-Cu₂ZnGeSe₄/60 nm TiO₂/ITO cell stack and of the individual stack components: (i) ZnO:Al front electrode, (ii) 60 nm TiO₂/ITO back electrode after H₂Se exposure at 450°C, (iii) EVAP-Cu₂ZnGeSe₄ absorber (as-deposited on quartz glass substrate) compared to their spectral sum := (i) + (ii) + (iii).



1

2 Figure 15: The efficiency of a four-terminal mechanically stacked geometry c-Si bottom+top
 3 cell as function of the light transmitted through the top cell (T for $\lambda \geq hc/E_{g_{top}}$). As top cell,
 4 8 and 15 % CZGSe and 22 % CIGS cells are used. The horizontal dashed line indicates the
 5 efficiency of the c-Si bottom cell alone and serves as a performance reference. ❶ and ❷
 6 indicate the performance situation in 2015 ($\eta \approx 3\%$ and $T \approx 17\%$, calculated for measured
 7 transparency of CZGSe on TBC (ITO/TiO₂)) and 2018 (as reported in this publication: $\eta \approx$
 8 8% and $T \approx 40\%$). ❸ indicates a realistic performance scenario for which η and T have to
 9 be increased to 15 % and 60 %, respectively.

10

1 **SUPPLEMENTARY MATERIAL FOR**

2
3 **WIDE BAND GAP KESTERITE ABSORBERS FOR THIN FILM SOLAR CELLS:**
4 **POTENTIAL AND CHALLENGES FOR THEIR DEPLOYMENT IN TANDEM DEVICES**

5
6 Bart Vermang^{1,2,3}, Guy Brammertz^{1,2,3}, Marc Meuris^{1,2,3}, Thomas Schnabel⁴, Erik Ahlswede⁴,
7 Leo Choubrac⁵, Sylvie Harel⁵, Christophe Cardinaud⁵, Ludovic Arzel⁵, Nicolas Barreau⁵,
8 Joop van Deelen⁶, Pieter-Jan Bolt⁶, Patrice Bras⁷, Yi Ren⁷, Eric Jaremal⁷, Samira Khelifi^{8,9},
9 Sheng Yang⁸, Johan Lauwaert⁸, Maria Batuk¹⁰, Joke Hadermann¹⁰, Xeniya Kozina¹¹,
10 Evelyn Handick¹¹, Claudia Hartmann¹¹, Dominic Gerlach¹², Asahiko Matsuda¹³,
11 Shigenori Ueda^{14,15}, Toyohiro Chikyow^{12,13}, Roberto Félix¹¹, Yufeng Zhang^{11,16},
12 Regan G. Wilks^{11,17}, and Marcus Bär^{11,17,18,19}

13
14 ¹imec division IMOMEc – partner in Solliance, Wetenschapspark 1, 3590 Diepenbeek,
15 Belgium

16 ²Hasselt University – partner in Solliance, Martelarenlaan 42, 3500 Hasselt, Belgium

17 ³EnergyVille, Thorpark 8320, 3600 Genk, Belgium

18 ⁴ZSW, Meitnerstrasse 1, 70563 Stuttgart, Germany

19 ⁵Institut des Matériaux Jean Rouxel (IMN), Université de Nantes, CNRS, 2 rue de la
20 Houssinière, 44322 Nantes, France

21 ⁶TNO – partner in Solliance, High Tech Campus 21, 5656 AE Eindhoven, The Netherlands

22 ⁷Midsummer AB, Elektronikhöjden 6, 175 43 Järfälla, Sweden

23 ⁸Department of Electronics and Information Systems (ELIS), Ghent University,
24 Technologiepark Zwijnaarde 15, 9052 Gent, Belgium

25 ⁹Department of Solid State Sciences, Ghent University, Krijgslaan 281-S1, 9000 Gent,
26 Belgium

27 ¹⁰Electron Microscopy for Materials Science (EMAT), University of Antwerp,
28 Groenenborgerlaan 171, 2020 Antwerp, Belgium

29 ¹¹Department Interface Design, Helmholtz-Zentrum Berlin für Materialien und Energie
30 GmbH (HZB), Hahn-Meitner-Platz 1, 14109 Berlin, Germany

1 ¹²International Center for Materials Nanoarchitectonics (MANA), National Institute for
2 Materials Science (NIMS), 1-1 Namiki, Tsukuba, Ibaraki 305-0044, Japan

3 ¹³Research and Services Division of Materials Data and Integrated System (MaDIS), National
4 Institute for Materials Science (NIMS), 1-1 Namiki, Tsukuba, Ibaraki 305-0044, Japan

5 ¹⁴Synchrotron X-ray Station at SPring-8, National Institute for Materials Science (NIMS), 1-1-
6 I Kouto, Sayo-cho, Hyogo 679-5148, Japan

7 ¹⁵Research Center for Advanced Measurement and Characterization, National Institute for
8 Materials Science (NIMS), 1-2-1, Sengen, Tsukuba, Ibaraki 305-0047, Japan

9 ¹⁶College of Physical Science and Technology, Xiamen University (XMU), 361005, Xiamen,
10 China

11 ¹⁷Energy Materials In-Situ Laboratory Berlin (EMIL), Helmholtz-Zentrum Berlin für
12 Materialien und Energie GmbH (HZB), Albert-Einstein-Str. 15, 12489, Berlin, Germany

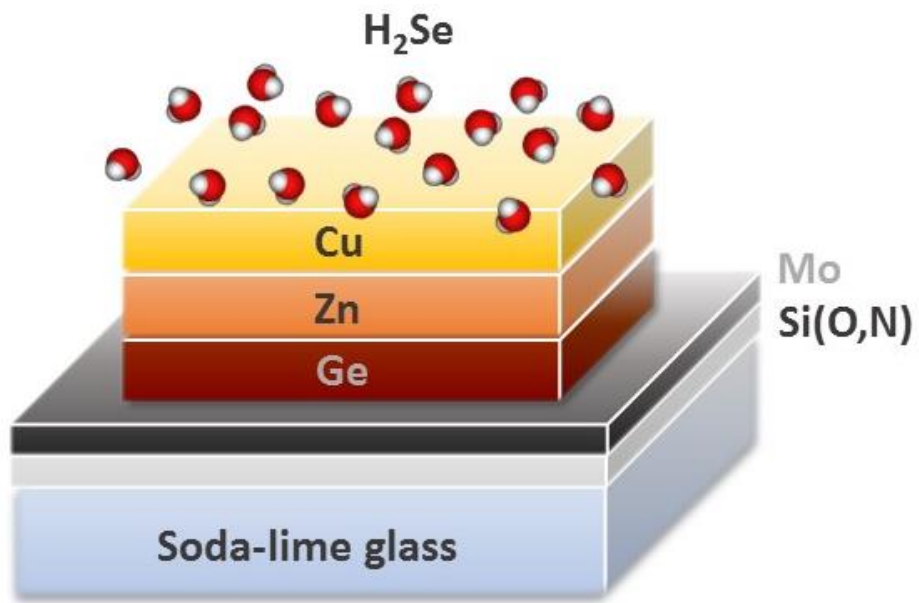
13 ¹⁸Department of Chemistry and Pharmacy, Friedrich-Alexander-Universität Erlangen-
14 Nürnberg, 91058 Erlangen, Germany

15 ¹⁹Helmholtz-Institute Erlangen-Nürnberg for Renewable Energy (HI ERN), 12489 Berlin,
16 Germany

17

18 CORRESPONDING AUTHOR – Bart Vermang, Martelarenlaan 42, 3500 Hasselt, Belgium

19



1
2
3
4

Figure S1: Schematic representation of the two-step selenization process used for EVAP-Cu₂ZnGeSe₄ absorber fabrication.

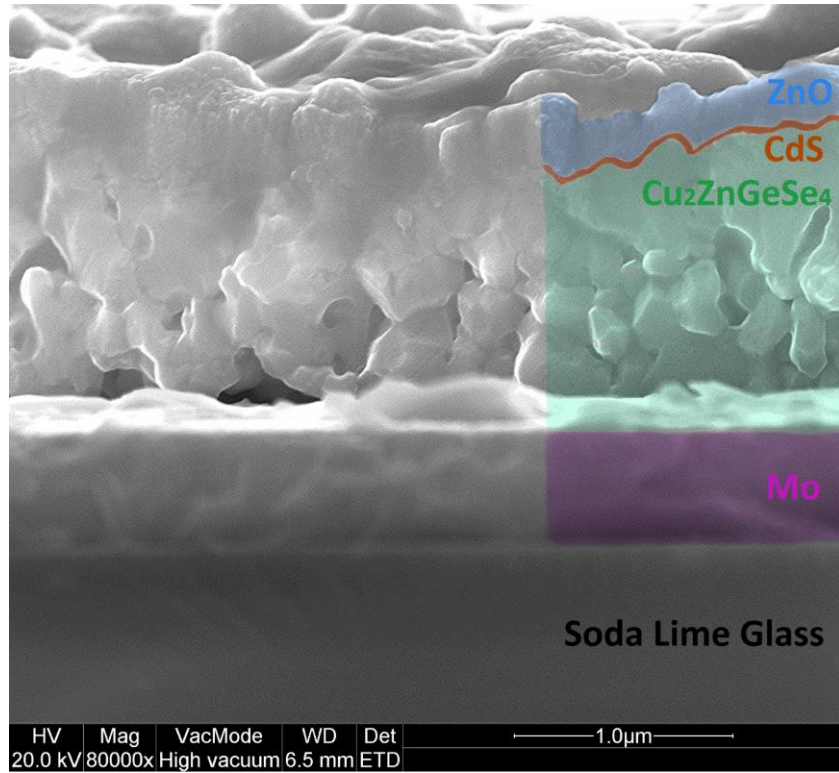
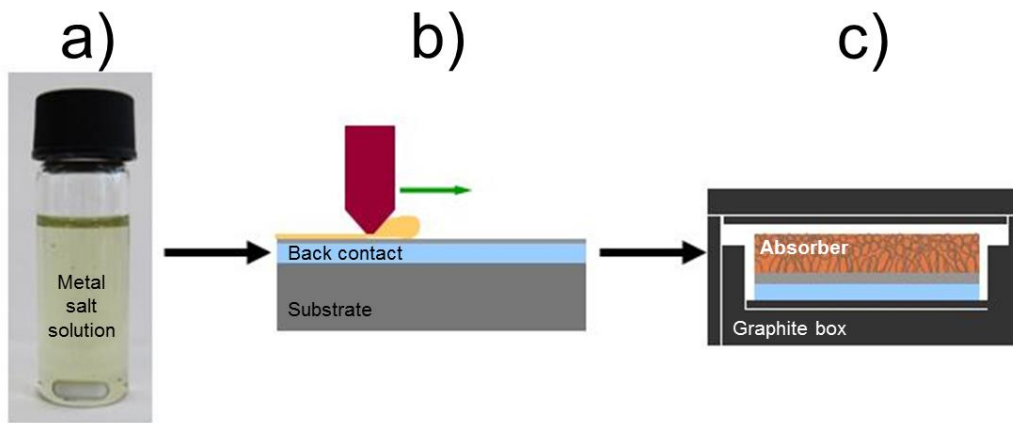


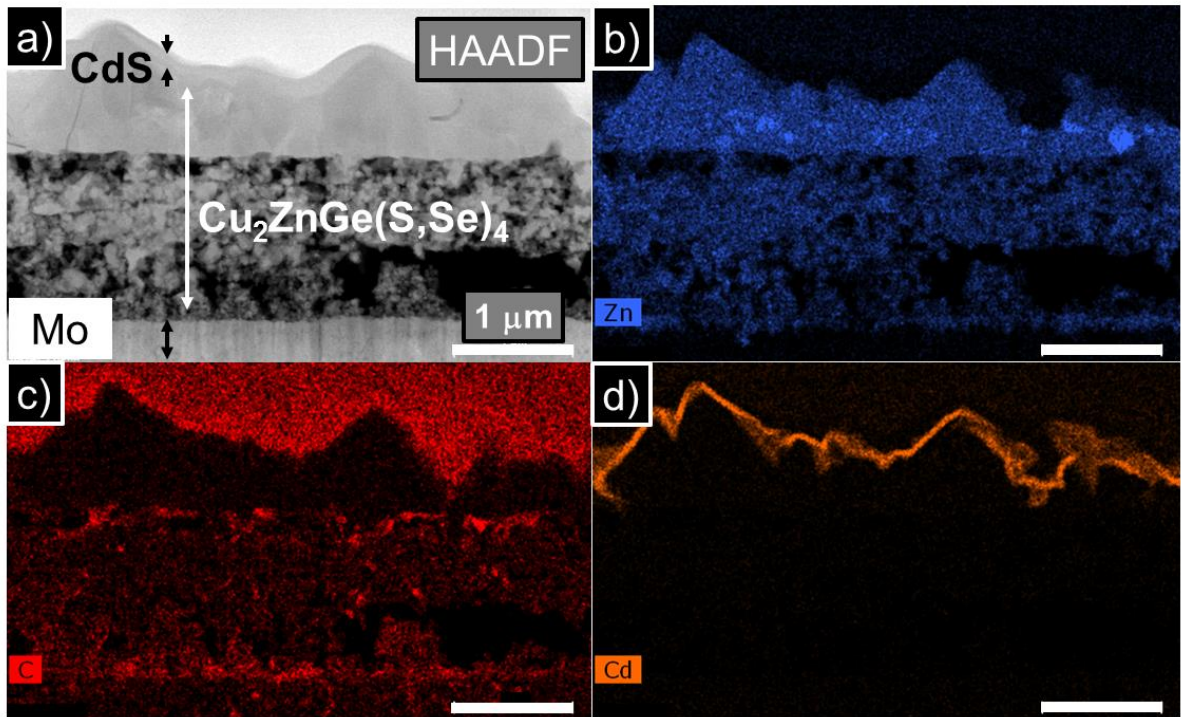
Figure S2: Cross-section scanning electron microscopy image of a finished EVAP- $\text{Cu}_2\text{ZnGeSe}_4$ solar cell sample, showing the grain morphology of the absorber and contact layer.



1

2 Figure S3: Schematic illustration of the solution process of preparing a SOL-Cu₂ZnGe(S,Se)₄
 3 absorber: a) metal salt solution, b) doctor blade coating, c) annealing in Se atmosphere.

4



1
2
3
4
5

Figure S4: Cross-section high angle annular dark field (HAADF) STEM image of a SOL- $\text{Cu}_2\text{ZnGe}(\text{S,Se})_4$ -based solar cell with CdS buffer and ZnO window (a), and the elemental maps of Zn (b), C (c) and Cd (d).

Buffer layer	V _{OC} (mV)	FF (%)	J _{sc} (mA/cm ²)	E _G (eV)	Eff. (%)
CBD CdS ^[17]	617	54.1	18.0	1.47	6.0
CBD Zn(O,S)	512	51.2	17.7	1.51	4.6
rf-Zn(O _{0.6} S _{0.4}) ^[17]	730	48.3	13.0	1.54	4.6
ALCVD In ₂ S ₃ ^[17]	469	48.2	14.9	1.49-1.54	3.4
Co-evap. CdIn ₂ S ₄ ^[17]	354	49.6	14.7	1.44	2.6

1

2 Table S1: Electrical parameters for the most efficient buffer/SOL-Cu₂ZnGe(S,Se)₄ solar cells.

3

Parameter	ZnO:Al	CdS	Cu ₂ ZnGe(S,Se) ₄	MoSe ₂ ^[31]	MoO ₃ ^[32]
d (μm)	0.120	0.050	1-2	0.04-0.10	0.04
E _G (eV)	3.3	2.4	1.47-1.5	1.1	2.85
χ (eV)	4.4	4.2	4.54	4.14	2.6
μ _n (cm ² /V.s)	100	100	10	100	100
μ _p (cm ² /V.s)	25	25	2	25	20
N _d (cm ⁻³)	10 ¹⁸	3×10 ¹⁷	-	-	-
N _A (cm ⁻³)	-	-	2×10 ¹⁵ / 10 ¹⁶ ^(○)	10 ¹⁶	10 ¹⁸
R _s (Ω.cm ⁻¹)	4.7 / 0.5 ^(○)				
R _{sh} (Ω.cm ⁻¹)	365 / 800 ^(○)				

1

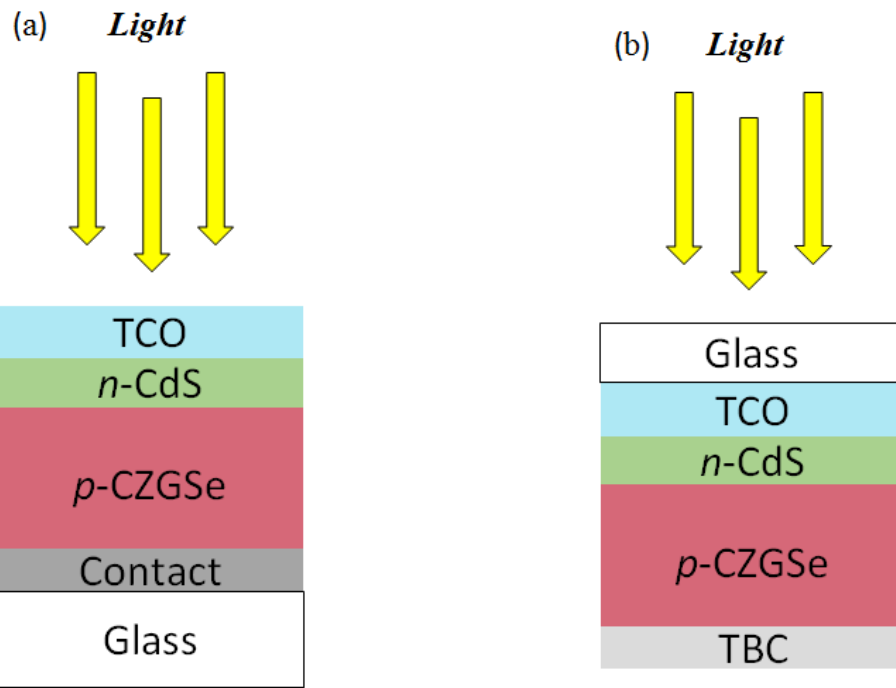
2

Table S2: Parameters used in the simulations at standard solar cell test conditions.

3

^(○) Optimized parameters.

4



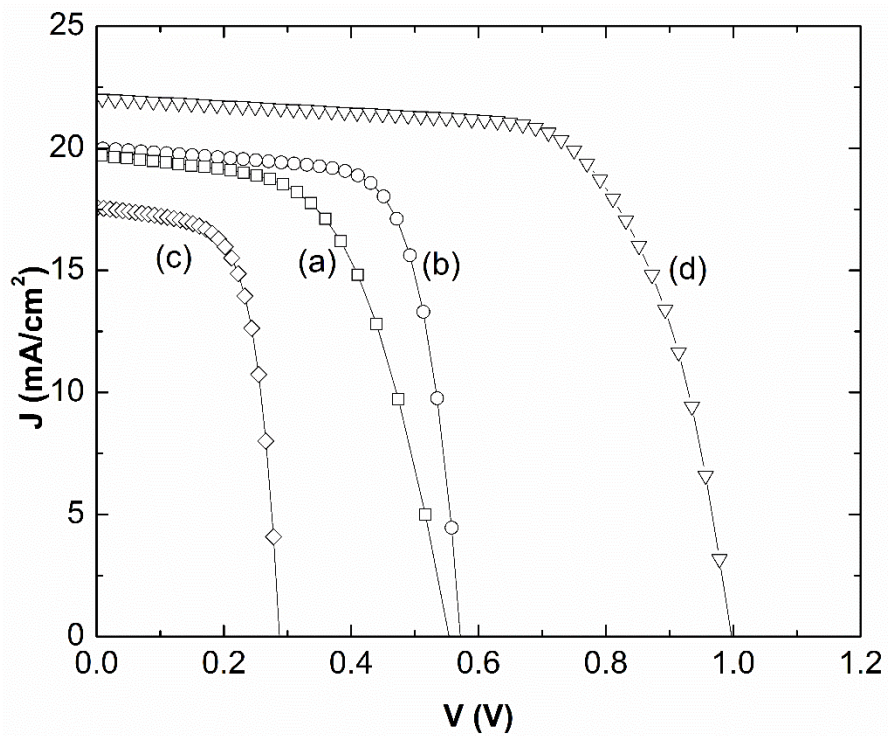
1

2

Figure S5: Schematic of the two different configurations considered in the device simulations: (a) substrate and (b) superstrate.

3

4



1

2 Figure S6: Calculated $J(V)$ curves for different substrate/superstrate configurations: (a)

3 substrate = $\text{Cu}_2\text{ZnGe}(\text{S},\text{Se})_4/\text{MoSe}_2/\text{Mo}/\text{glass}$, (b) same configuration as (a) but using

4 optimized device simulation parameters (see Table S2), (c) superstrate =

5 $\text{Cu}_2\text{ZnGe}(\text{S},\text{Se})_4/\text{TCO}$, and (d) superstrate = $\text{Cu}_2\text{ZnGe}(\text{S},\text{Se})_4/\text{MoO}_3/\text{TCO}$. For

6 configurations (c) and (d) also optimized parameters were used in the device simulation.

7